nature communications

Article

https://doi.org/10.1038/s41467-024-53733-0

PTPRK regulates glycolysis and de novo lipogenesis to promote hepatocyte metabolic reprogramming in obesity

Received: 13 February 2024

Accepted: 22 October 2024

Published online: 04 November 2024

Check for updates

Eduardo H. Gilglioni[1], Ao Li[1], Wadsen St-Pierre-Wijckmans[1], Tzu-Keng Shen[1,2,3,4], Israel Pérez-Chávez[1,2,3,4], Garnik Hovhannisyan[1], Michela Lisjak[1], Javier Negueruela[1], Valerie Vandenbempt[1], Julia Bauzá-Martinez[5,6], Jose M. Herranz[7], Daria Ezeriņa[2,3,4], Stéphane Demine[1], Zheng Feng[1], Thibaut Vignane[8], Lukas Otero Sanchez[9,10], Flavia Lambertucci[1], Alena Prašnická[1], Jacques Devière[9,10], David C. Hay[11], Jose A. Encinar[12], Sumeet Pal Singh[13], Joris Messens[2,3,4], Milos R. Filipovic[8], Hayley J. Sharpe[14], Eric Trépo[9,10], Wei Wu[5,6,15,16] & Esteban N. Gurzov[1,17]

Fat accumulation, de novo lipogenesis, and glycolysis are key drivers of hepatocyte reprogramming and the consequent metabolic dysfunction-associated steatotic liver disease (MASLD). Here we report that obesity leads to dysregulated expression of hepatic protein-tyrosine phosphatases (PTPs). PTPRK was found to be increased in steatotic hepatocytes in both humans and mice, and correlates positively with PPARγ-induced lipogenic signaling. High-fat-fed PTPRK knockout male and female mice have lower weight gain and reduced hepatic fat accumulation. Phosphoproteomic analysis in primary hepatocytes and hepatic metabolomics identified fructose-1,6-bisphosphatase 1 and glycolysis as PTPRK targets in metabolic reprogramming. Mechanistically, PTPRK-induced glycolysis enhances PPARγ and lipogenesis in hepatocytes. Silencing PTPRK in liver cancer cell lines reduces colony-forming capacity and high-fat-fed PTPRK knockout mice exposed to a hepatic carcinogen develop smaller tumours. Our study defines the role of PTPRK in the regulation of hepatic glycolysis, lipid metabolism, and tumour development in obesity.

Consumption of processed industrialized foods with high caloric density and reduced energy expenditure results in nutrient overload. In response, cells adapt by storing energy in the form of triglycerides, generating adipose tissue expansion and ectopic fat deposition in organs such as the liver. The presence of a lipid-rich environment has deleterious pathological consequences, including insulin resistance and dyslipidaemia. If not resolved, it can evolve into metabolic dysfunction-associated steatotic liver disease (MASLD), affecting a quarter of the global adult population[1,2]. Metabolic dysfunction-associated steatohepatitis (MASH), a severe necro-inflammatory form of MASLD, poses a significant health problem[3,4]. Moreover, MASLD has emerged as a leading cause of hepatocellular carcinoma (HCC), a highly heterogeneous and aggressive malignancy[5].

The liver is central to nutrient sensing and has a significant impact during obesity, resulting in abnormal lipid accumulation and hepatocyte metabolic reprogramming. This involves the intricate reorganization of anabolic and catabolic processes, all under the transcriptional control of nutrient-sensitive receptors. In the context

A full list of affiliations appears at the end of the paper. e-mail: esteban.gurzov@ulb.be

of obesity and HCC, several transcription factors, including PPARs, SREBP1c, ChREBP, and HIF, participate in the reshaping of metabolic pathways[3,4]. In addition, post-translational modifications, including phosphorylation of protein tyrosine residues, are dysregulated in nutrient overload and obesity[6].

Hepatic expression of Protein Tyrosine Phosphatases (PTPs) is affected in steatotic livers and MASH. PTPs were conventionally perceived as enzymes responsible for terminating or modulating signals initiated by tyrosine kinases[7]. Accumulating evidence reveals their potential as signal propagators[6,8]. For example, PTPN2 facilitates signaling through both STAT1 and STAT3, exerting distinct influences on MASH and HCC[9]. Oxidative inactivation of PTPN2 induces an insulin-STAT5-IGF-1-growth hormone pathway in conditions of selective insulin resistance, contributing to obesity[10]. Receptor-type PTPs (RPTPs) are transmembrane enzymes adapted to sense and transduce extracellular cues into intracellular catalytic events[11]. In obesity, inflammatory signals induce the expression of PTPRG in the liver[12]. Deleting or overexpressing PTPRG enhances or suppresses hepatic insulin sensitivity, respectively[12]. However, a lack of comprehensive studies to understand liver PTPomes in obesity means that the role of PTPs in regulatory mechanisms and their potential use as biomarkers or therapeutic targets remain largely unexplored.

PTPRK is a transmembrane receptor belonging to the R2B subfamily of RPTPs, known to engage in homophilic interactions and localizes to cell-cell contacts[11]. Cell adhesion proteins have been proposed as PTPRK substrates, and accumulating data associate PTPRK with several human diseases[13–15]. The regulation of PTPRK involves a proteolytic cascade (furin, ADAM10, and γ-secretase), potentially releasing the intracellular catalytic domain to interact and dephosphorylate proteins in the cytoplasm or nucleus[16]. PTPRK is transcriptionally regulated by transforming growth factor-β (TGF-β) and Notch signaling[17]. Despite its potential in cell signaling, the downstream events regulated by PTPRK remain unknown. In this study, we demonstrated that PTPRK is upregulated in fatty hepatocytes and investigated its role in obesity-associated liver dysfunction. PTPRK deficiency leads to severe metabolic changes in hepatocytes, culminating in reduced diet-induced obesity and hepatic fat accumulation in mice. We identified fructose-1,6-bisphosphatase 1 (FBP1), a gluconeogenic enzyme, as PTPRK target, bearing significant implications for glucose metabolism and liver tumor growth. These findings underscore the pivotal role of PTPRK as key driver in the metabolic reprogramming of hepatocytes induced by obesity.

Results

Hepatic PTP expression is dysregulated in obesity-associated liver dysfunction

The presence and potential contribution of PTP expression in the progression to MASLD in obesity and the development of HCC remains unknown. Therefore, we conducted a comprehensive analysis of the complete proteome and PTP expression patterns, using liquid chromatography-tandem mass spectrometry (LC-MS/MS) analysis of human liver samples (Fig. 1a). The cohort included liver biopsies obtained from individuals exhibiting varying degrees of liver disease, encompassing simple steatosis, MASH, HCC, and control samples from individuals without evidence of liver damage (healthy liver). The heatmap illustrating the total proteome alterations showed variations in protein expression and sample heterogeneity across different stages of liver dysfunction (Supplementary Fig. 1a). All samples except 1 HCC and 2 MASH passed total proteome quality control for heatmap analysis. HCC was not considered for pathway analysis due to the low number of samples. KEGG pathway analyses between healthy, steatosis and MASH samples revealed that several protein modifications are related to metabolic dynamics. When comparing steatosis with healthy livers, we observed activation of oxidative phosphorylation, starch, and sucrose metabolism. We also observed activation of glutathione metabolism, alongside the suppression of the tight junction pathway (Supplementary Fig. 1b). Activated pathways in MASH included ECM receptor interaction, oxidative phosphorylation, and focal adhesion (Supplementary Fig. 1c). Conversely, pathways related to the pentose phosphate pathway (PPP), purine metabolism, histidine metabolism, and cysteine and methionine metabolism were suppressed. Further, comparing MASH to steatosis, oxidative phosphorylation was suppressed in MASH, while ECM receptor interaction, focal adhesion, and ribosome pathways were activated (Supplementary Fig. 1d). Proteome analysis revealed key enzymes involved in fatty acid uptake and metabolism, CD36, CPT1, and SCD, upregulated in steatosis and MASH samples (Fig. 1b). Among the samples, 18 out of the 37 human PTP proteins were identified with 10 being RPTPs (Fig. 1c). Analysis of the PTPome revealed that samples within the same disease stage displayed similar expression patterns for the majority of PTPs detected (Fig. 1d), while analysis of RPTPs and non-receptor protein tyrosine phosphatases (PTPNs) revealed opposing patterns across the stages of the disease (Fig. 1e). Several PTPNs were downregulated with the exception of increased PTPN7 (expressed mainly in immune cells) in MASH (Fig. 1d–f). RPTPs generally exhibited low expression levels in healthy liver samples but showed marked upregulation in steatosis and MASH. PTPRF was decreased by MASH, while PTPRB and PTPRJ were not affected by steatosis or MASH. PTPRK, PTPRE, PTPRM, PTPRF, and PTPRA (PTPRA-1) were elevated in steatosis and MASH (Fig. 1f). Single-cell RNA sequencing of healthy-obese livers[18] revealed that PTPRK is the most abundant RPTP in hepatocytes, followed by PTPRG and PTPRM, with PTPRE mainly found in dendritic cells (Fig. 1g and Supplementary Fig. 1e). Additionally, RPTP displayed comparable mRNA patterns in the E-MEXP-3291 dataset (Fig. 1h). Immunohistochemistry (IHC) analyses in human liver samples showed that PTPRK levels were higher in steatosis and MASH, whereas healthy liver displayed relatively lower expression. The PTPRK intracellular domain localized within various cellular regions, including the nucleus of steatotic hepatocytes (Fig. 1i). Consistent with this result, PTPRK-GFP intracellular domain localized in the cytoplasm and nucleus in transfected HepG2 cells (Fig. 1j), as previously shown[16]. Full-length PTPRK-GFP localizes within intracellular vesicles, and forms cell-to-cell homophilic interactions at the plasma membrane (Fig. 1j). The striking remodeling of PTPomes with disease onset indicates a potential causative role in fat accumulation and liver dysfunction.

Hepatocyte PTPRK is induced in obesity and positively correlates with PPARγ in mouse models and primary hepatocytes

To gain functional insights into the hepatic role of PTPRK we took advantage of obesogenic mouse models. C57BL/6N mice were exposed to diet-induced obesity over a 12-week period. Both high-fat diet (HFD) and high-fat, high-fructose high-cholesterol diet (HFHFHCD) resulted in a noticeable increase in body weight (Fig. 2a), primarily attributed to increased fat body mass (Fig. 2b). This was accompanied by elevated fasting insulin levels (Fig. 2c), glucose intolerance (Fig. 2d), and reduced insulin sensitivity (Fig. 2e). PTPRK is expressed in hepatocytes, but undetectable in subcutaneous and visceral adipose tissues or muscle (Fig. 2f). Mice fed with HFHFHCD exhibited a greater liver weight, liver-to-body weight ratio, and liver fat mass compared to the control group (Fig. 2g, h), consistent with a more advanced stage of fatty liver development. PTPRK protein expression is enhanced in HFD and HFHFHCD-fed mice livers, accompanied by PPARγ upregulation (Fig. 2i), a master regulator of lipid accumulation in hepatocytes. Adenovirus-mediated overexpression of PTPRK in mouse livers resulted in a concomitant increase in PPARγ levels (Fig. 2j). In line with these results, hepatic PTPRK transcript levels in human livers positively correlate with PPARγ (Supplementary Fig. 2a). These findings demonstrate a consistent involvement of PTPRK in lipid metabolism and diet-induced liver dysfunction.

https://doi.org/10.1038/s41467-024-53733-0

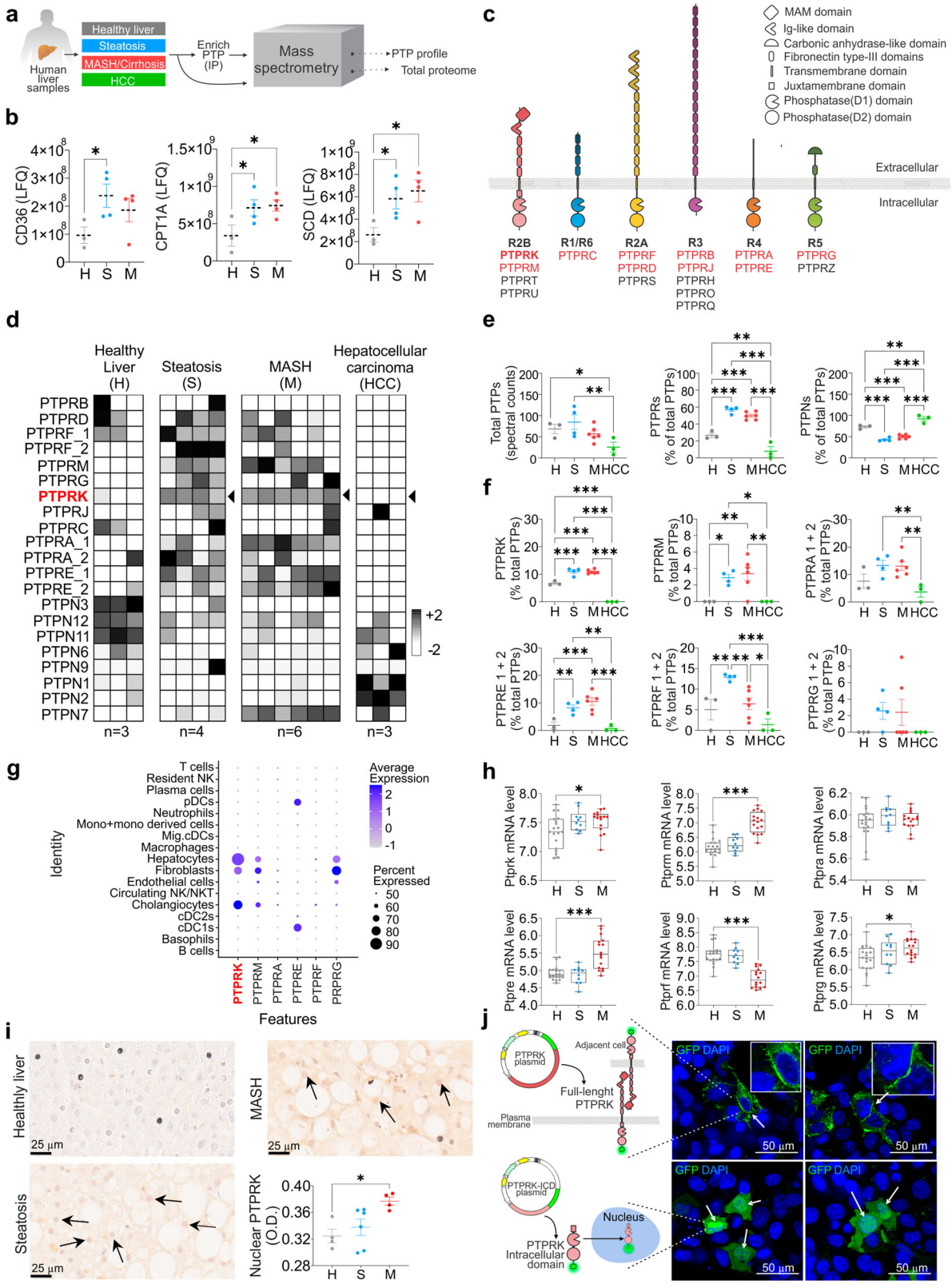

Extended culture of primary mouse hepatocytes resulted in a loss of differentiation, causing changes in metabolic pathways similar to those observed in vivo during the progression of MASLD. We observed a gradual accumulation of lipid droplets in the cytosol of hepatocytes (Fig. 2k). This was accompanied with increased protein levels of PTPRK and PPARγ (Fig. 2l). Acute and chronic treatment of primary hepatocytes with insulin or pro-inflammatory cytokines TNFα, IL6 or IFNγ did not affect PTPRK expression (Supplementary Fig. 2b–e). NOTCH2 is significantly increased in primary hepatocytes over time in culture (Supplementary Fig. 2f), and the administration of the Notch signaling inhibitor GSIXX effectively prevented upregulation of both PTPRK and PPARγ in a dose-dependent manner (Fig. 2m). Treatment with lipopolysaccharide (LPS) significantly increased both PTPRK and PPARγ transcripts and protein levels (Fig. 2n, o). Dimethyloxalylglycine

Fig. 1 | Enhanced PTPRK expression in human livers with steatosis or metabolic dysfunction-associated steatohepatitis (MASH). a Methodological approach schematic illustrating the quantification of protein tyrosine phosphatase (PTP) profile and total proteome in human livers. **b** Quantification of lipid metabolism-related proteins using label-free quantification (LFQ) in healthy (H, $n = 3$), steatosis (S, $n = 4$) and MASH (M, $n = 4$) livers. **c** Schematic representation of receptor-type PTP (RPTP)s and their characteristic domains. RPTPs detected by mass spectrometry are indicated in red. **d** Heat map showing the hepatic PTP profile. **e** Spectral counts of total PTPs and the proportional contribution of receptor and non-receptor PTPs (H: $n = 3$; S: $n = 4$; M: $n = 6$; HCC: $n = 3$). **f** The proportional protein contribution of PTPRK and other receptor PTPs to the total identified PTPs is shown (H: $n = 3$; S: $n = 4$; M: $n = 6$; HCC: $n = 3$). **g** Data extracted from the GSE192740 single-cell RNA-seq dataset showing receptor PTP mRNA expression in liver cells. **h** Data extracted from the E-MEXP-3291 dataset showing RPTP mRNA levels using genome-wide microarray analysis and presented as box plots showing median with whiskers at minimum and maximum values (H: $n = 19$; S: $n = 10$; M: $n = 16$). **i** Representative immunohistochemistry (IHC) images displaying PTPRK staining and quantitative results for nuclear PTPRK (H: $n = 4$; S: $n = 6$; M: $n = 4$). Scale bar = 25 µm. **j** Cellular localization of recombinant PTPRK in HepG2 cells. Representative confocal images showing the full-length (top row) and intracellular domain (ICD, bottom row) of PTPRK protein tagged with mGreenLantern (GFP, green). Nuclei were stained with DAPI (blue). Scale bar = 50 µm. In **b**, **e**, **f**, **i** results are shown as means ± SEM. Statistical analyses were done using one-way ANOVA (**b**, **e**, **f**, **i**) or Kruskal–Wallis test (**h**) and denoted as $^{*}p < 0.05$, $^{**}p < 0.01$, $^{***}p < 0.001$. Source data are provided as a Source Data file.

(DMOG) induces hypoxia-inducible factor (HIF)-mediated adaptation to low oxygen levels, gene transcription, and reprogramming cellular metabolism. HIF induction in primary mouse hepatocytes reduced PTPRK and PPARγ expression levels (Fig. 2p). Together, these experiments provided compelling evidence of a positive correlation between PTPRK and PPARγ in hepatocytes, which can be regulated by diverse signaling pathways.

PTPRK deletion protects against diet-induced obesity, insulin resistance, and hepatic steatosis in mice

To directly evaluate the metabolic relevance of PTPRK, we conducted loss-of-function studies using 8-week-old *Ptprk*$^{-/-}$ and *Ptprk*$^{+/+}$ mice subjected to either an HFHFHCD or a chow diet. PTPRK deficiency had minimal impact on body weight gain and fat accumulation in chow-fed mice (Supplementary Fig. 3a–d). Glucose and insulin tolerance tests performed at 8 weeks of age showed no differences between *Ptprk*$^{-/-}$ and *Ptprk*$^{+/+}$ mice (Supplementary Fig. 3e–h). At 20 weeks, *Ptprk*$^{-/-}$ mice showed improved glucose homeostasis (Supplementary Fig. 3i–l). The intake of chow diet was not affected (Supplementary Fig. 3m, n). After 12 weeks of HFHFHCD feeding, *Ptprk*$^{+/+}$ mice developed obesity, characterized by substantial increases in body weight, fat mass, circulating insulin levels, homeostasis model assessment of insulin resistance (HOMA-IR), glucose intolerance and insulin resistance (Fig. 3a–h and Supplementary Fig. 4a, b). Strikingly, *Ptprk*$^{-/-}$ mice displayed resistance to HFHFHCD-induced obesity, as their body weight, fat mass, circulating insulin levels, HOMA-IR, glucose sensitivity and insulin resistance were all significantly lower (Fig. 3a–h). This protective effect was particularly prominent in female mice.

Consistent with the metabolic analyses, PTPRK-deficient mice exhibited elevated energy expenditure, specifically during the dark cycle (Supplementary Fig. 4c). *Ptprk*$^{-/-}$ mice also displayed increased VO_2 levels during the night, and the respiratory exchange ratio (RER) showed a downward trend (Supplementary Fig. 4c). No significant disparities were noted in ambulatory activity or food and water intake (Supplementary Fig. 4c, d). The analysis of food intake over a span of 12 weeks revealed no disparities in males, but lower levels in female *Ptprk*$^{-/-}$ mice, resulting in lower cumulative energy intake (Supplementary Fig. 4e, f). PTPRK deficiency did not result in altered lipid excretion through feces (Supplementary Fig. 4g), suggesting that the reduced weight observed in *Ptprk*$^{-/-}$ mice is not related to changes in intestinal fat absorption. *Ptprk*$^{-/-}$ livers exhibited significantly higher induction of p-IR and p-AKT compared to *Ptprk*$^{+/+}$ mice in response to insulin (Fig. 3i). The phosphorylation levels induced by insulin on IR and AKT displayed no discernible differences in primary hepatocytes (Supplementary Fig. 5a), indicating that PTPRK does not directly affect IR phosphorylation. We observed a significant reduction in hepatic lipid accumulation within the livers of *Ptprk*$^{-/-}$ mice (Fig. 3j–o). Collectively, these findings demonstrate that while PTPRK-deficiency exerts minimal influence on normal development, it confers robust protection against diet-induced obesity, steatosis, and insulin resistance.

PTPRK expression shapes nutrient-driven metabolic reprogramming in hepatocytes

Having established that PTPRK plays a major metabolic role in obesity, we next sought to define the lipogenic pathways affected in HFHFHCD-fed mice. Immunoblot analysis showed that *Ptprk*$^{-/-}$ mice exhibited lower levels of hepatic PPARγ (Fig. 4a, b), while no differences were observed in subcutaneous and visceral adipose tissues (Fig. 4c, d and Supplementary Fig. 5b, c). We observed significantly reduced expression of Pparγ2 transcripts in *Ptprk*$^{-/-}$ mice, while Pparγ1 was unaffected (Fig. 4e). Key lipogenic enzymes, namely Scd1, Acly, Acc, and Fasn mRNA were downregulated in *Ptprk*$^{-/-}$ mice (Fig. 4e). Immunoblot analysis confirmed diminished levels of ACC and FASN in *Ptprk*$^{-/-}$ mice (Fig. 4a, b). In addition, transcription factors governing fat metabolism, SREBP1c and ChREBP, also exhibited decreased expression in *Ptprk*$^{-/-}$ livers (Fig. 4a, b). Individual feeding behaviors may influence observed differences in SREBP1, ChREBPα, and other metabolic proteins.

Next, we used adenoviral-mediated upregulation of PTPRK in 4-week HFHFHCD fed mice and observed a significant increase in hepatic PPARγ expression following adenoviral infection (Fig. 4f). Adenoviral PTPRK overexpression reverted the hepatic phenotype of obese *Ptprk*$^{-/-}$ mice, including increased liver weight, liver-to-body weight ratio, and liver fat mass (Fig. 4g). Histological examination of liver sections and lipid measurements revealed increased lipid deposition following PTPRK overexpression (Fig. 4h). These results demonstrate that hepatic PTPRK overexpression effectively reverses key phenotypic characteristics observed in PTPRK-deficient mice. Primary hepatocytes with reduced PTPRK levels (heterozygous) or complete deletion (knockouts) showed reduced kinetics of STAT1 phosphorylation in response to IFNγ (Supplementary Fig. 5d, e). STAT1 and Activator Protein 1 (AP-1) play a pivotal role in driving PPARγ expression and lipid accumulation within the liver[19,20]. Notably, we observed significantly lower levels of c-Fos/AP-1 in *Ptprk*$^{-/-}$ livers (Supplementary Fig. 5f). Taken together, our results suggest that PTPRK acts upstream of transcriptional regulators of de novo lipogenesis and lipid metabolism in obesity.

Phosphoproteomic analysis revealed FBP1 as a PTPRK substrate in hepatocytes during steatosis

To explore the mechanisms by which PTPRK inactivation in hepatocytes might drive the development of steatosis, we performed unbiased transcriptome and proteomic analysis. Hepatocytes were isolated and separated based on their fat content (Fig. 5a). Immunoblot analysis of high-fat content hepatocytes further established the positive correlation between PTPRK and PPARγ (Fig. 5b). Steatotic PTPRK-deficient hepatocytes have reduced Cd36 expression, a crucial PPARγ target in cellular fatty acid uptake (Fig. 5c). In contrast, Cpt1, facilitating long-chain fatty acid transport for mitochondrial β-oxidation, displayed an opposing pattern, with higher expression in *Ptprk*$^{-/-}$ hepatocytes (Fig. 5c). We performed RNA-Seq analysis in low/high fat *Ptprk*$^{-/-}$ and *Ptprk*$^{+/+}$ hepatocytes (Supplementary Fig. 6a). Volcano plot analysis revealed that the predominant significant differences

https://doi.org/10.1038/s41467-024-53733-0

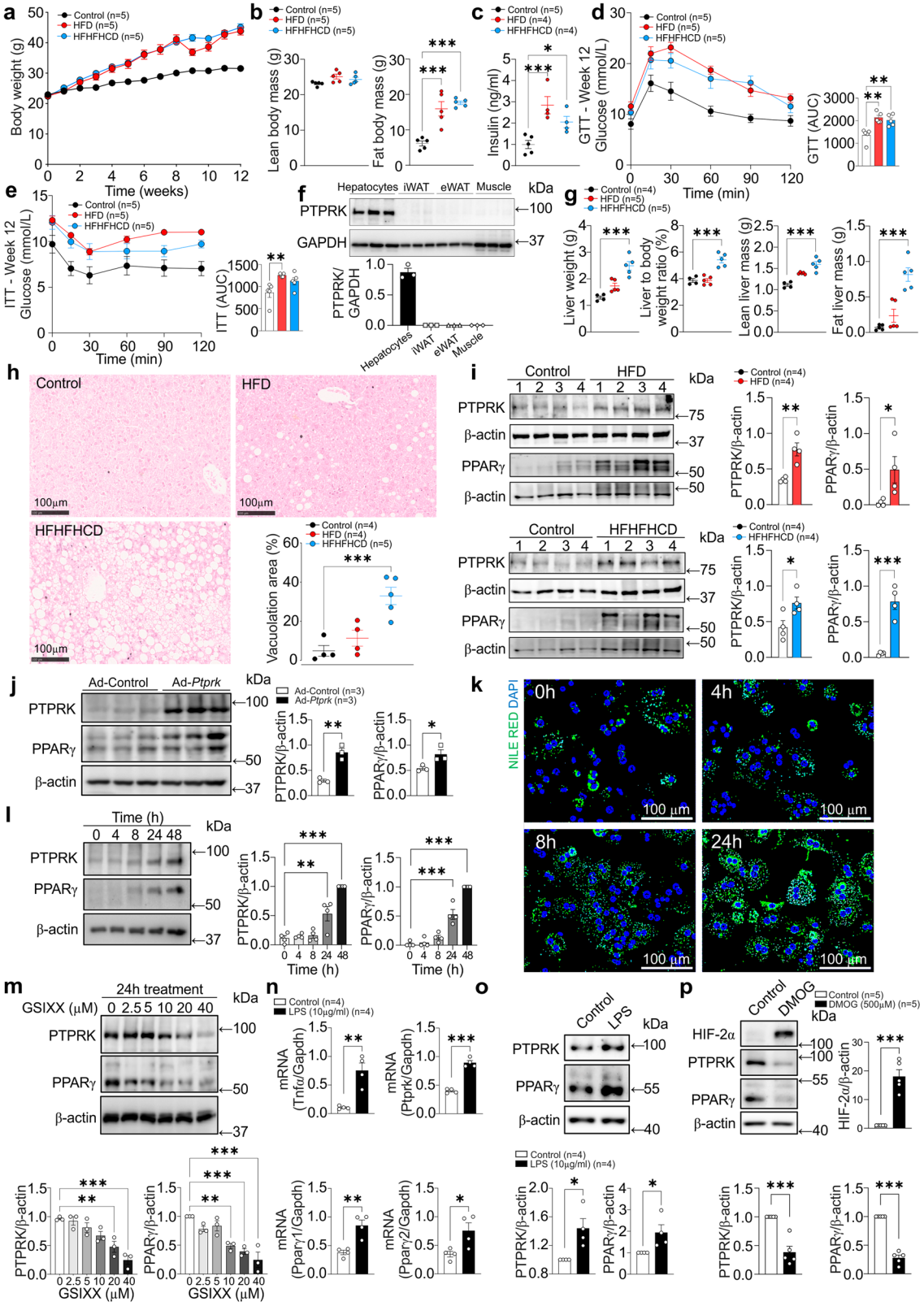

occurred among genes upregulated in low-fat hepatocytes compared to high-fat hepatocytes within the same genotype (Supplementary Fig. 6b, c). In contrast, only a limited number of genes exhibited significant transcriptional alterations resulting from PTPRK deletion in low-fat or high-fat hepatocytes (Supplementary Fig. 6d, e). We also observed reduced PPAR signaling in *Ptprk*$^{-/-}$ hepatocytes (Fig. 5d). Comparison of low-fat to high-fat *Ptprk*$^{+/+}$ hepatocytes revealed enriched pathways, including cell adhesion molecules, MAPK signaling, PI3K-AKT signaling, cytokine interaction, and chemokine signaling (Fig. 5e). In *Ptprk*$^{-/-}$ hepatocytes, the same comparison highlighted pathways including gap junction and ECM receptor interaction, which are likely related to the role of PTPRK at the cellular interface.

We next performed proteomics and phosphoproteomic analysis of hepatocytes with high-fat content (Supplementary Fig. 6f). The

Fig. 2 | Hepatocyte PTPRK is induced by Notch signaling and LPS, correlating positively with PPARγ in obese mouse models and primary hepatocytes. a–**e** 8-week-old male C57BL6N mice were fed either a high-fat diet (HFD) or a high-fat high-fructose high-cholesterol diet (HFHFHCD) for 12 weeks. **a** Body weight was measured weekly, **b** body composition, and **c** fasting insulinemia were measured after 12 weeks of feeding. Mice underwent **d** glucose and **e** insulin tolerance tests after 12 weeks of diet. **f** Primary hepatocytes, inguinal white adipose tissue (iWAT), epididymal white adipose tissue (eWAT), and gastrocnemius (muscle) from 3 mice per group were harvested for immunoblot analysis. **g** The livers of the mice fed HFHFHCD and HFD for 12 weeks were extracted and assessed for hepatic weight and composition. **h** Histological analysis was conducted to quantify hepatic vacuolation area. Scale bar = 100 µm. **i** Immunoblot analysis shows hepatic levels of PTPRK and PPARγ. **j** 8-week-old male C57BL6N mice receiving a chow (control) diet were transduced with an adenoviral vector to induce PTPRK overexpression (Ad-*Ptprk*). Two weeks later, immunoblot analysis was performed in liver samples to assess the levels of PTPRK and PPARγ. **k** Primary mouse hepatocytes were cultured overnight under standard conditions and fixed at different time points for Nile Red and DAPI staining. Scale bar = 100 µm. **l** Immunoblot analysis was performed on primary mouse hepatocytes collected at different time points as indicated ($n = 4$). **m** Primary mouse hepatocytes were cultured overnight and treated with different concentrations of GSIXX ($n = 3$). Immunoblot analysis was used to evaluate the expression of PTPRK and PPARγ. **n**, **o** Primary mouse hepatocytes were cultured overnight and treated with lipopolysaccharide (LPS) for 24 h. Gene expression was analyzed by quantitative PCR (**n**) or immunoblotting (**o**). **p** Primary mouse hepatocytes were cultured overnight and treated with dimethyloxalylglycine (DMOG) for 24 h. Immunoblotting was performed for HIF2α, PTPRK, and PPARγ. Each individual value represents independent hepatocyte preparations from different mice. In **a**–**j**, **l**–**p** results are shown as means ± SEM. Statistical analyses were done using two-tailed unpaired Student's *t* test (**i**, **j**, **n**–**p**) or using one-way ANOVA (**b**–**e**, **g**, **h**, **l**, **m**). Statistical significance is denoted as $^{*}p < 0.05$, $^{**}p < 0.01$, $^{***}p < 0.001$. Source data are provided as a Source Data file.

Venn diagram illustrates that 1148 proteins show modifications in both the phosphoproteomic and total proteome datasets. This suggests an intricate relationship between these protein datasets, indicating regulatory mechanisms acting at the translational level and post-translationally through phosphorylation (Supplementary Fig. 6f). The heatmap displays diverse protein changes between *Ptprk*$^{-/-}$ and *Ptprk*$^{+/+}$ hepatocytes (Fig. 5f), revealing their dynamic response. In *Ptprk*$^{-/-}$ hepatocytes, an upregulation of specific proteins has been observed, reflecting a complex interplay of molecular events associated with altered mitochondrial function and redox balance, closely linked to cellular metabolic reprogramming (Fig. 5g). Enriched pathways include metabolism, phagosome, and biosynthesis of unsaturated fatty acids (Fig. 5h). PTPRK-deficiency increases phosphorylated residues across various proteins (Fig. 5i). These changes are associated with crucial pathways, including insulin signaling, mTOR pathway, AMPK signaling, insulin resistance, glucagon signaling, adherens junctions, and biosynthesis of amino acids (Fig. 5j).

A total of 2572 phosphosites were significantly upregulated in *Ptprk*$^{-/-}$ hepatocytes compared with 258 found at lower levels (Supplementary Fig. 6g). Phosphotyrosine residues of CPSM (pY162), CH10 (pY76), WASL (pY253), GSTP1 (pY8), and FBP1 (pY265, pY216) were increased in *Ptprk*$^{-/-}$ hepatocyte (Fig. 5k). The focussed analysis of FBP1, a hepatic tumor suppressor[21], revealed changes also at the positions pS273, pS248, pY265, pY245 and pY216 in *Ptprk*$^{-/-}$ steatotic hepatocytes (Fig. 5l). FBP1 is a key enzyme active in gluconeogenesis and glucose homeostasis. Structural modeling highlights conserved helical regions (Fig. 5m) that engage with the PTPRK D2 domain (Fig. 5n), placing phosphorylated tyrosine residues near the PTPRK catalytic D1 domain. Computational simulations confirmed PTPRK and tyrosine phosphorylated complex predictions with a range of different assemblies (Supplementary Fig. 7a–f). We confirmed PTPRK-FBP1 interaction by Bio-Layer Interferometry (Supplementary Fig. 7g) and immunoprecipitation analysis with FBP1 wild-type and tyrosine Y265, Y245 and Y216 mutants (Supplementary Fig. 7h–j). Pervanadate-treated hepatocyte lysates, combined with recombinant PTPRK intracellular domain (PTPRK-ICD), demonstrated FBP1 dephosphorylation (Fig. 5o). We analyzed glycolysis dynamics using HYlight, a biosensor designed to track real-time changes in intracellular levels of the FBP1 substrate, fructose 1,6-bisphosphate[22]. We observed lower fructose 1,6-bisphosphate levels in *Ptprk*$^{-/-}$ hepatocytes when stimulated with glucose (Fig. 5p). Our results demonstrate the dynamic interplay between PTPRK and FBP1, significantly impacting glucose metabolism.

Deletion of PTPRK induces metabolic reprogramming in the liver during diet-induced obesity

To assess the importance of hepatic PTPRK in glycolytic control, we cultured primary mouse hepatocytes after adenovirus-mediated PTPRK overexpression or silencing (Fig. 6a). Glucose-starved hepatocytes overexpressing PTPRK displayed increased glycolytic activity. This was evident in the extracellular acidification rates measured after acute glucose injection and after oligomycin blockade of mitochondrial respiration (Fig. 6b). Hepatocytes with PTPRK overexpression exhibited increased lipid droplet accumulation (Fig. 6c). In addition, lipid droplet accumulation occurred to a greater extent in PTPRK overexpressing hepatocytes after fatty acid administration (Fig. 6c). PTPRK overexpression induced PPARγ, increased glucose consumption and fat accumulation in high-glucose exposed primary hepatocytes (Fig. 6d–f). We hypothesized that elevated glycolysis downstream PTPRK induces PPARγ and channels pyruvate toward acetyl-CoA synthesis, triggering de novo lipogenesis (Fig. 6g). PPARγ knockdown suppressed PTPRK-mediated fat accumulation (Fig. 6h, i). In agreement with our hypothesis, FBP1 inhibition enhanced PPARγ and fat accumulation in PTPRK knocked-down hepatocytes (Fig. 6j, k). Moreover, inhibition of glucose oxidation resulted in decreased PPARγ expression, while PTPRK expression was not affected (Supplementary Fig. 8a).

We performed metabolite tracing experiments to compare the effects of PTPRK overexpression and silencing on glycolytic flux in hepatocytes (Fig. 7). Hexoses bisphosphate, primarily represented by fructose 1,6-bisphosphate, exhibited increased abundance and fractional contribution in PTPRK overexpression. Furthermore, dihydroxyacetone phosphate and glyceraldehyde-3-phosphate, both downstream products of fructose 1,6-bisphosphate, showed increased abundance in PTPRK overexpression, as well as phosphoenolpyruvate, indicating enhanced conversion of glyceraldehyde 3-phosphate through the latter stages of glycolysis (Fig. 7).

We next sought to validate our results in human hepatocytes. *PTPRK*$^{-/-}$ and *PTPRK*$^{+/+}$ human embryonic stem cells (hESC) were differentiated into hepatocyte-like cells (HLCs, Supplementary Fig. 8b–d). Deletion of PTPRK did not affect hESC hepatocyte differentiation nor the ability of HLCs to produce and secrete albumin (Supplementary Fig. 8b–d). Similar to mouse hepatocytes, PTPRK-deficient HLCs exhibited a reduced glycolytic rate following glucose stimulation (Supplementary Fig. 8e).

Liver metabolites from *Ptprk*$^{-/-}$ and *Ptprk*$^{+/+}$ mice fed HFHFHCD for 12 weeks were quantified by mass spectrometry (Fig. 8a). *Ptprk*$^{-/-}$ livers showed decreased levels of dihydroxyacetone phosphate and glyceraldehyde-3-phosphate, with a corresponding reduction in the lactate/pyruvate ratio. *Ptprk*$^{-/-}$ livers displayed elevated α-ketoglutarate levels and increased pyruvate. Despite elevated pyruvate levels, *Ptprk*$^{-/-}$ livers exhibited reduced concentrations of acetyl-CoA, and increased free coenzyme A compared to *Ptprk*$^{+/+}$. This aligns with our findings of decreased levels of pyruvate dehydrogenase phosphatase in *Ptprk*$^{-/-}$ mice, while no differences were observed for pyruvate dehydrogenase kinase (Supplementary Fig. 8f). PTPRK deficiency also led to heightened pentose phosphate pathway (PPP) intermediates, particularly

https://doi.org/10.1038/s41467-024-53733-0

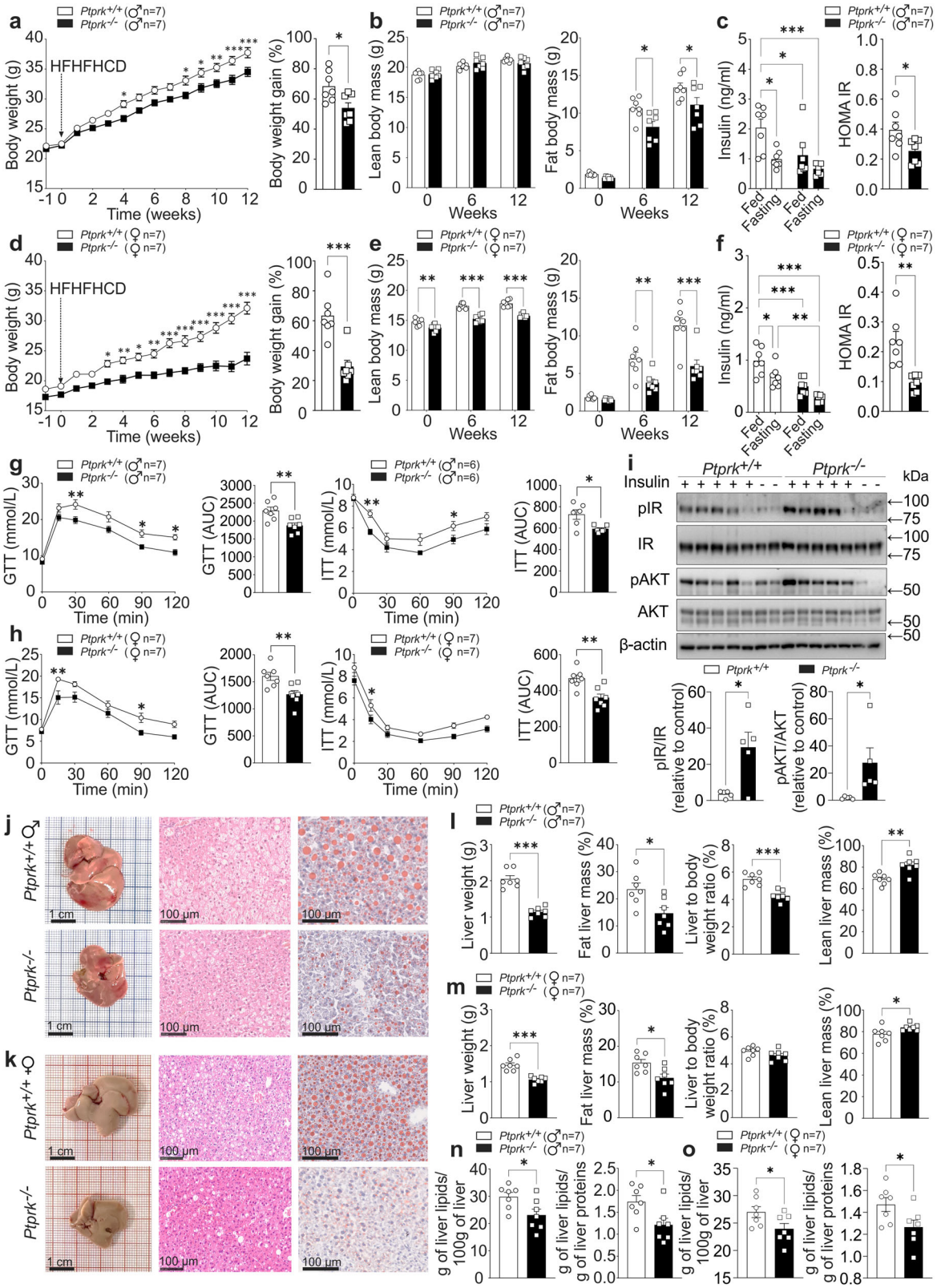

ribulose-5-phosphate and erythrose 4-phosphate (Fig. 8a). Enhancing the flux through the PPP could reinforce essential production of reducing equivalents, and increase oxidative stress management. Parallel to shifts in lactate-to-pyruvate ratio, *Ptprk*$^{-/-}$ livers unveiled elevated GSSG (Fig. 8a) and methionine sulfoxide levels (Supplementary Fig. 8g). The ratio of the classical redox indicators NAD$^+$/NADH, NADP$^+$/NADPH, and GSSG/GSH showed no significant changes (Supplementary Fig. 8h), although the total levels of NADP$^+$ were significantly lower in *Ptprk*$^{-/-}$ (Fig. 8a). No differences were found in phosphorylated adenine nucleotides (ATP, ADP and AMP, Supplementary Fig. 8i) and amino acids (Supplementary Fig. 8j). Several factors may contribute to dissociation between enzyme levels with their substrate and product abundance, including phosphorylation and other post-translational modifications. We observed heightened

Fig. 3 | PTPRK deletion confers protection against diet-induced obesity, insulin resistance, and hepatic steatosis. a–h Male (♂) and female (♀) C57BL6N *Ptprk*$^{+/+}$ and *Ptprk*$^{-/-}$ mice, aged 8 weeks, were subjected to a high-fat, high-fructose, high-cholesterol diet (HFHFHCD) for 12 weeks. Body weight (**a**, **d**) was measured weekly. Body composition was measured before (week 0) and after 6 and 12 weeks of HFHFHCD feeding (**b**, **e**). Insulinemia was measured after 12 weeks of HFHFHCD feeding in the fed state and after 6 h of fasting (**c**, **f**). Glucose and insulin tolerance tests were performed after 12 weeks of HFHFHCD feeding (**g**, **h**). **i** At the end of HFHFHCD feeding, insulin ($n = 5$) or PBS ($n = 2$) was administered to female mice 10 min prior to liver collection. Immunoblot analysis was employed to examine the expression of pIR and pAKT in the liver. **j–o** Liver samples were analyzed to assess fat accumulation through histological examination, scale bar = 1 cm or 100 µm as indicated. **j**, **k** Measurements of liver weight and composition (**l**, **m**), and total liver lipid extraction (**n**, **o**). In **a–i**, **l–o** results are shown as means ± SEM. Statistical analyses were done using two-tailed unpaired Student's *t* test (**g–i**, **l–n**) or using two-way ANOVA (**a–f**). Statistical significance is denoted as $^{*}p < 0.05$, $^{**}p < 0.01$, $^{***}p < 0.001$. Source data are provided as a Source Data file.

expression of Pck1, a pivotal gluconeogenic driver, in *Ptprk*$^{-/-}$ livers (Fig. 8b), consistent with lower glycolysis. *Ptprk*$^{-/-}$ female mice, subjected to a 12-week HFHFHCD obesogenic diet, exhibited elevated blood glucose levels compared to *Ptprk*$^{+/+}$ after pyruvate injection, supporting a shift to a more gluconeogenic state upon PTPRK deletion (Fig. 8c). Together, these observations indicate that PTPRK leads to steatosis indirectly by stimulating glycolytic activity and PPARγ induction and directly by accelerating fatty acid esterification and lipid droplet formation in response to fatty acids.

PTPRK contributes to hepatocyte transformation in obesity-associated HCC

Glycolytic and gluconeogenic proteins, including FBP1 (Supplementary Fig. 9a), contribute to HCC development[21]. We observed a stratification pattern based on PTPRK mRNA expression levels in human samples (Fig. 9a) that bifurcated into two distinct clusters: one characterized by high PTPRK expression and the other marked by low PTPRK expression. Normal liver samples uniformly exhibited low PTPRK expression, while in the context of MASH, peritumour, and tumor conditions, high PTPRK expression was correlated with elevated hepatic expression of glycolytic genes. The analysis of all liver samples and the focused analysis of tumor samples revealed a positive correlation between elevated PTPRK expression and hepatic expression of lipogenic genes (Fig. 9b). The enriched pathways associated with elevated PTPRK expression in liver tumor samples, as defined through KEGG pathway enrichment analysis, underscored the activation of fatty acid metabolism, type 1 diabetes mellitus, glycolysis/gluconeogenesis, TCA cycle, primary bile acid biosynthesis, biosynthesis of unsaturated fatty acids, PPAR signaling pathway, steroid biosynthesis, and oxidative phosphorylation (Fig. 9c).

To investigate the implications of PTPRK deletion in the context of liver cancer, diethylnitrosamine (DEN), a potent hepatocarcinogen, was administered by a single injection into *Ptprk*$^{-/-}$ and *Ptprk*$^{+/+}$ mice aged two weeks and fed a chow or HFHFHCD (starting at 6 weeks of age). *Ptprk*$^{-/-}$ male and female mice showed reduced body weight and fat accumulation compared with *Ptprk*$^{+/+}$ mice on chow or HFHFHCD (Fig. 9d, g and Supplementary Fig. 9b, e). Livers from *Ptprk*$^{-/-}$ male and female mice were smaller and had reduced absolute hepatic lipid content (Fig. 9d, g and Supplementary Fig. 9b, e). PTPRK deficiency reduced DEN-mediated tumor numbers in obese females (Supplementary Fig. 9e). Macroscopic evaluation showed reduced tumor size in *Ptprk*$^{-/-}$ obese males and lean females (Fig. 9g and Supplementary Fig. 9b). This was confirmed by histological analysis of liver sections, where *Ptprk*$^{-/-}$ tumors exhibited significantly diminished dimensions and reduced fat accumulation regardless of sex or diet (Fig. 9e, f, h, i and Supplementary Fig. 9c, d, f, g). In line with these findings, silencing of PTPRK using siRNA in HepG2, HLE, and Huh6 cells led to substantial attenuation of colony-forming capacity (Fig. 9j, k and Supplementary Fig. 9h). Overall, our experiments support the oncogenic role of PTPRK in promoting rapid hepatic tumor growth.

Discussion

Modern diets and lifestyles pose a chronic challenge to the ancestral mechanisms designed to control energy balance in humans. In the present study, we observed increased expression of hepatic RPTPs in steatosis and MASH, suggesting an adaptive response. The upregulation of PTPRK may serve as a part of a compensatory mechanism to mitigate the impact of disrupted cell adhesion components and mechanotransduction in fat-loaded hepatocytes. PTPRK seems to play a pivotal role in disease progression, influencing glycolysis, de novo lipogenesis signaling, and associated metabolic pathways.

We demonstrated that the upregulation of hepatocyte PTPRK-PPARγ correlates with NOTCH2 activation and that the inhibition of Notch signaling suppresses PTPRK-PPARγ expression in hepatocytes[17,23]. In addition, LPS increased PTPRK-PPARγ, while HIF2α represses it. The metabolic phenotypes induced by HIF or PTPRK are similar, with increased glycolysis and triglyceride accumulation, albeit driven by different molecular mechanisms. Our results suggest that inflammation and hypoxia can influence PTPRK expression, potentially contributing to the differences observed in human liver samples. The correlation between elevated PTPRK expression and the activation of glycolytic and lipogenic genes is consistent with the role played by PTPRK in regulating these metabolic pathways.

Obesogenic diets lead to hepatic PTPRK overexpression, and global PTPRK knockout mice are resistant to diet-induced metabolic dysfunction. The absence of PTPRK resulted in delayed onset of obesity and steatosis with suppression of nutrient-sensitive transcription factors PPARγ, SREBP1c, and ChREBP, relevant for metabolic reprogramming[24,25]. We found that PTPRK deletion leads to c-Fos downregulation and lower STAT1 activation in response to IFNγ. Both c-Fos and STAT1 are known to promote PPARγ expression[19,20]. PTPRK-induced glycolysis contributes to increased PPARγ expression and lipogenesis. FBP1 inhibition enhanced PPARγ and fat accumulation in PTPRK-silenced hepatocytes. Inhibiting glucose oxidation suppresses PPARγ expression in hepatocytes without altering PTPRK expression, suggesting a downstream effect. A future study is required to determine the detailed mechanism of glycolysis-mediated PPARγ regulation.

Glucose oxidation provides the energy, metabolites, and reducing agents necessary for the execution of de novo lipogenesis and sustains a shift in fatty acid metabolism from a catabolic to an anabolic direction[26]. PTPRK deficiency results in lower expression of the PPARγ target gene CD36, a long-chain free fatty acid transporter that promotes the growth of HCC cells by increasing glycolysis[27]. In overnutrition, PTPRK mediates the shift towards glycolysis and fat storage. PTPRK deletion also protected mice against insulin resistance and hyperinsulinemia after obesogenic diet feeding. Hepatic PTPRK overexpression is sufficient to reverse the phenotype. Elevated insulin levels, insulin resistance, and excessive fat accumulation in hepatocytes are key drivers of metabolic reprogramming, fueling the phenotypic changes necessary for malignant transformation of hepatocytes[4,28].

In aerobic conditions, pyruvate and cytosolic NADH are readily oxidized in the mitochondria. However, as mitochondrial energy production meets cellular energy demand, counterregulatory mechanisms are activated to slow down the TCA cycle and mitochondrial function[29]. If the glycolytic activity remains active, an excessive supply of acetyl-CoA originating from pyruvate may

https://doi.org/10.1038/s41467-024-53733-0

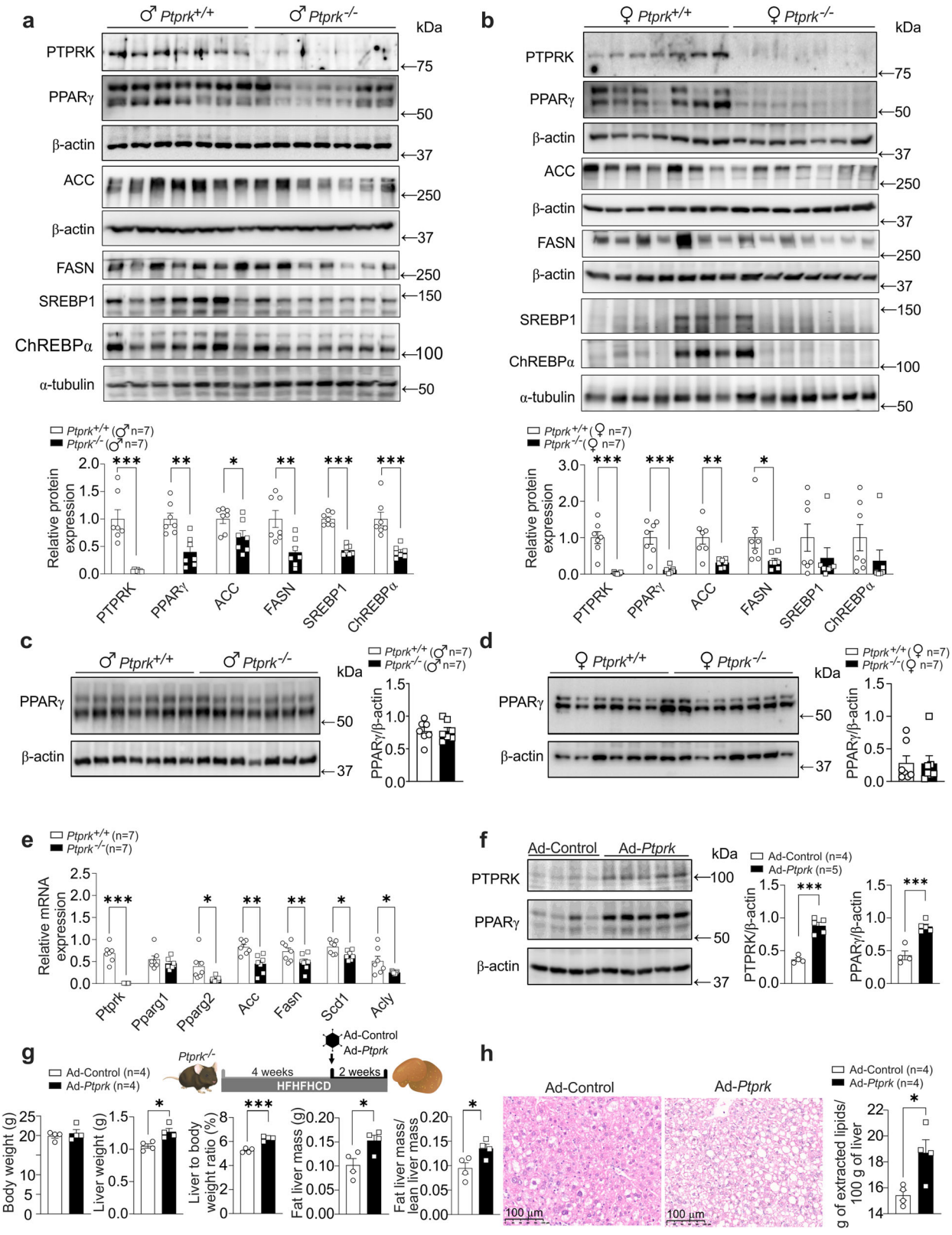

accumulate, along with increased pyruvate fermentation into lactate[30]. The accumulated acetyl-CoA is then converted to malonyl-CoA, serving as a substrate for de novo lipogenesis and an allosteric inhibitor of CPT1α[26]. We found that the metabolic balance is regulated by PTPRK and favored the conversion of pyruvate into acetyl-CoA by the pyruvate dehydrogenase complex. Indeed, we observed PTPRK-dependent increased lactate/pyruvate ratio, reduced PDHK1/PDP1 ratio, accumulation of acetyl-CoA, and upregulation of ACC and FASN. All these factors collectively contribute to the increased lipogenic capacity of PTPRK-expressing hepatocytes, ultimately resulting in higher steatosis.

Glycolytic and gluconeogenic rates are reciprocally regulated, and the suppression of gluconeogenic reactions favors glycolysis. The involvement of PTPRK in hepatic glucose metabolism is an important

Fig. 4 | PTPRK orchestrates the hepatic expression of metabolic enzymes and transcription factors promoting steatosis in mice fed an obesogenic diet. **a**, **b** Eight-week-old male (♂) and female (♀) C57BL6N *Ptprk*$^{+/+}$ and *Ptprk*$^{-/-}$ mice were exposed to a high-fat, high-fructose, high-cholesterol diet (HFHFHCD) for 12 weeks. Liver samples were analyzed by immunoblotting to examine the protein levels of PTPRK, PPARγ, ACC (Acetyl-CoA Carboxylase), FASN (Fatty Acid Synthase), SREBP1 (Sterol Regulatory Element-Binding Protein 1), and ChREBP (Carbohydrate Response Element-Binding Protein). **c**, **d** Subcutaneous (inguinal fat) white adipose tissues were collected for immunoblot analysis of PPARγ. **e** Female liver mRNA expression of Ptprk, Pparγ, Acc, Fasn, Scd1 (Stearoyl-CoA Desaturase 1), and Acly (ATP Citrate Lyase) was assessed. **f** Female mice were subjected to HFHFHCD for 4 weeks and were administered an adenoviral vector to induce PTPRK overexpression (Ad-*Ptprk*). After 2 weeks, liver samples were collected for immunoblot analysis of PTPRK and PPARγ. **g** Female PTPRK-knockout mice were subjected to HFHFHCD for 4 weeks and subsequently injected with Ad-*Ptprk*. After an additional 2 weeks of HFHFHCD, body weight was measured, and liver samples were collected for the evaluation of weight and composition. **h** Liver histological assessment and total lipid extraction were performed after PTPRK overexpression in female mice. Scale bar = 100 µm. In **a**–**h** results are shown as means ± SEM. Statistical analyses were done using two-tailed unpaired Student's *t* test (**a**–**h**). Statistical significance is indicated as $^{*}p < 0.05$, $^{**}p < 0.01$, $^{***}p < 0.001$. Source data are provided as a Source Data file.

determinant of the metabolic phenotype of PTPRK knockout mice and the outcome of liver tumor formation experiments. Discrepancies in the role of PTPRK in tumor development and growth in extrahepatic tissues[31] may be due to the PTPRK–FBP1 regulation and its hepatic role in gluconeogenesis. Our experiments revealed that pyruvate and α-ketoglutarate are elevated in PTPRK knockout mice. α-ketoglutarate is a TCA cycle metabolite, that can supply carbons for gluconeogenesis; however, its accumulation reduces liver gluconeogenesis[32] and is associated with cancer suppression mechanisms[33]. The build-up of these gluconeogenic substrates indicates that even with a higher gluconeogenic capacity, the livers of PTPRK knockout mice still possess regulatory mechanisms to prevent uncontrolled gluconeogenesis. In line with this interpretation, hyperglycemia was not observed in PTPRK knockout mice, but higher glucose production was found during the pyruvate tolerance test, in which animals were fasted to stimulate gluconeogenesis.

Fat-loaded hepatocytes isolated from PTPRK knockout mice showed an accumulation of phosphorylated FBP1. Metabolomics and real-time detection of fructose 1,6-bisphosphate levels in primary hepatocytes lacking PTPRK revealed lower levels after glucose stimulation. Lower fructose 1,6-bisphosphate levels during glycolysis may also be a direct implication of the FBP1 tyrosine phosphorylation status. Thus, the observed outcome implies a futile cycle between FBP1 and PFK1 activities during glycolysis and optimized glucose production during gluconeogenesis. The substrate cycling at this step of glycolysis leads to wasteful ATP consumption[34], in agreement with the observed increased energy expenditure in PTPRK knockout mice and the substantial disparities observed for fat accumulation despite minor differences in food intake. Further research is needed to explore the precise implications of tyrosine phosphorylation on FBP1. It is crucial to identify the tyrosine kinases responsible for FBP1 phosphorylation and to examine the potential role of substrate cycling in glycolysis in maintaining energy homeostasis. Additionally, we cannot rule out direct or indirect regulation of additional enzymes by PTPRK in the glycolytic pathway that contribute to the phenotype.

Besides PTPRK, several classical PTPs present promising therapeutic opportunities. However, developing selective and bioavailable PTP inhibitors has proved challenging[35]. Recent studies have shown the effectiveness of competitive inhibitors for closely related PTPN2 and PTPN1[36,37]. RPTPs can additionally be inhibited by inducing their dimerization. For example, antibodies targeting PTPRD ectodomains induce protein dimerization and degradation, thereby suppressing PTPRD-dependent cell invasion in a metastatic breast cancer cell line[38]. PTPRG regulates hepatic inflammation and insulin resistance in obese and T2D[12]. Our study demonstrated a different role for PTPRK in dysregulation of hepatic glycolysis and lipid metabolism. Both PTPRG and PTPRK are potential therapeutic targets for mitigating liver complications in obesity-related disorders. Therapeutic options for end-stage liver diseases are limited[39]. Our proteomics analysis and RNA-Seq data suggest that PTPRK overexpression in HCC is not universal but rather patient-dependent. PTPRK inhibitors may hold potential in high-expressing PTPRK livers as an alternative or adjuvant treatment for obesity-associated liver dysfunction in personalized medicine. A future study using a larger cohort of human liver samples will allow the assessment of PTPRK expression and putative stratification according to gender, BMI, and disease.

In conclusion, PTPRK expression is increased in diseased human and mouse livers. Elevated hepatic PTPRK expression triggers heightened glycolysis, culminating in the activation of PPARγ and the stimulation of de novo lipogenesis. In mice, genetic PTPRK inhibition offers protection against the rapid development of liver dysfunction associated with obesogenic diet. Therefore, PTPRK emerges as a dual role player—serving as a biomarker for hepatic metabolic adaptations that influence the risk of metabolic liver disease and as a potential target for the development of therapies.

Methods

Liver samples were collected after approval of the Hôpital Erasme Ethics Committee (Brussels, Belgium). Written informed consent was obtained from each participant. The study was conducted with the approved human ethics by the Comité d'Ethique hospitalo-facultaire Erasme Université libre de Bruxelles (PI Gurzov approval Ref P2019/498). Mice were housed and managed in compliance with the Belgian Regulations for Animal Care, and the animal protocols underwent approval from the Commision d'Ethicque du Bien-Être Animal (CEBEA), Faculté de Médecine, Université libre de Bruxelles (dossier No. 732).

Reagents

Human insulin solution, sodium pyruvate, sodium palmitate, oleic acid, bovine serum albumin, 2-deoxy-D-glucose, D-glucose, $^{13}C_6$-glucose, mannoheptulose, DMOG, and LPS were obtained from Sigma-Aldrich. Recombinant murine IFNγ (315-05-100ug, PeproTech) and recombinant human IL6 (206-IL-010, R&D Systems) and FBP1 inhibitor (5-Chloro-2-(N-(2,5-dichlorobenzenesulfonamido))-benzoxazole, Santa Cruz Biotechnology) were used for in vitro experiments, while insulin ProZinc (NDC 0010-4499-01, Boehringer Ingelheim, Rhein, Germany) was used for in vivo experiments.

Human samples

We studied 19 biopsy specimens of patients undergoing a liver biopsy for medical reasons. The clinical characteristics of these patients are shown in Supplementary Table 1.

Extraction of proteins from human liver biopsies, enrichment of PTPs, and proteomics analysis

Frozen human liver biopsies were subjected to disruption using beads beating and sonication. Lysates were treated with lysis buffer containing 10% glycerol, 1% NP-40, cOmplete™EDTA-free protease inhibitor cocktail (Roche Diagnostics), and 1× phosphatase inhibitor (Sigma-Aldrich). After sonication, centrifugation at 20,000 × *g* for 1 h at 4 °C separated insoluble debris, retaining the supernatant for total proteome analysis. The obtained lysates were enzymatically digested using trypsin, targeting C-terminal lysine and arginine residues, except

https://doi.org/10.1038/s41467-024-53733-0

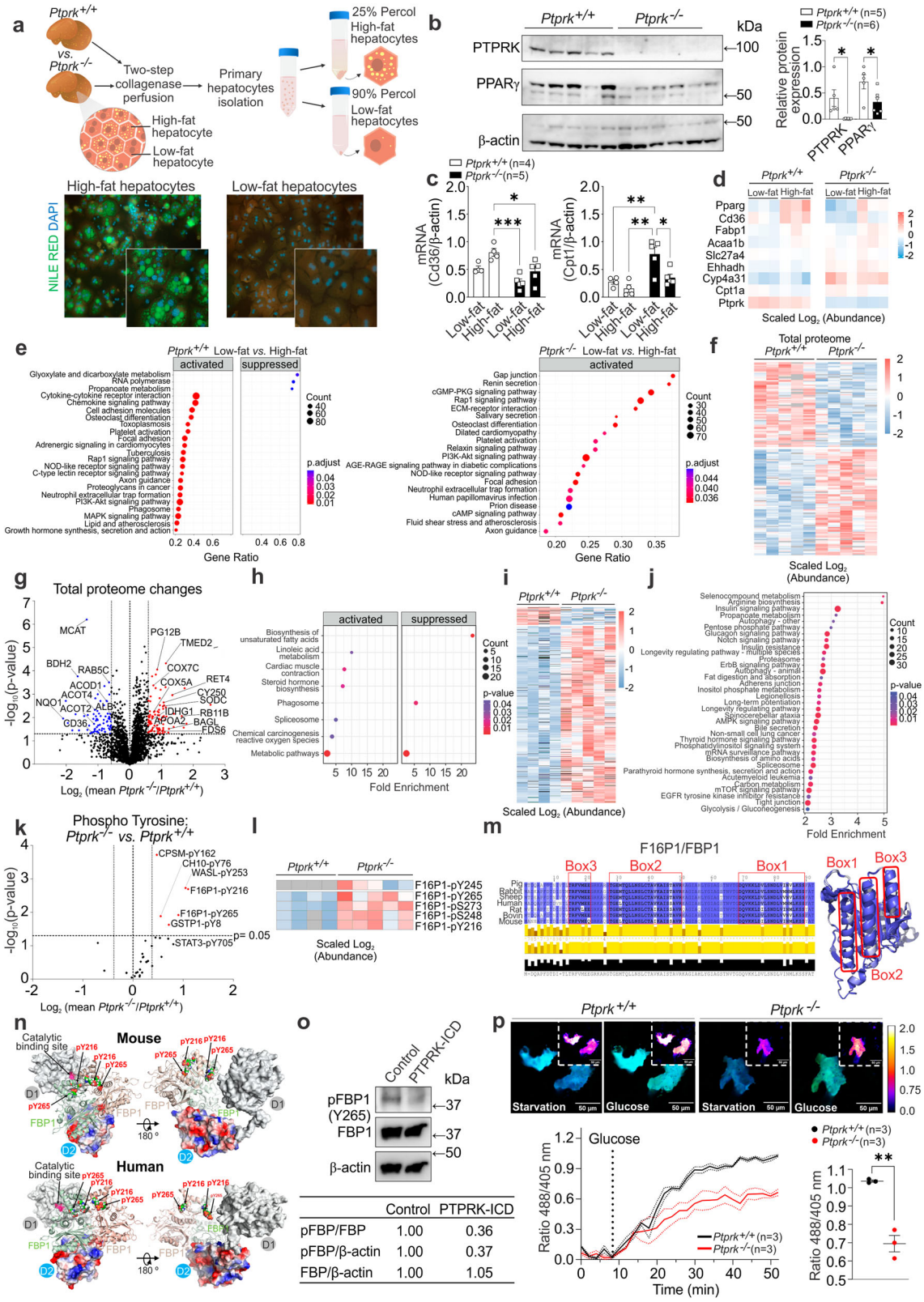

when adjacent to a C-terminal proline. Purification of the resulting peptides was performed using reverse-phase Sep-Pak C-18 cartridges, removing salts and buffers. By employing a strategy that explores the oxidation of cysteine in the catalytic site of PTPs, peptides containing cysteine residues within the PTP signature motif HCX5R were enriched through immunoprecipitation. Immunoprecipitated peptides, resuspended in 0.2% formic acid, were injected in triplicate for LC-MS/MS analysis. A 40-min reverse-phase gradient separation on UHPLC 1290 (Agilent Technologies) was followed by analysis on an Orbitrap Q Exactive HF mass spectrometer (Thermo Fisher Scientific), with MS scans spanning the 375–1500 m/z range at 60,000 resolution. Data were acquired in Data-Dependent Acquisition mode, selecting the top 7 precursor ions for HCD fragmentation, followed by MS/MS analysis at 30,000 resolution. MaxQuant (version 2.0.3.0) processed the

Fig. 5 | Transcriptome, proteome, and protein phosphorylation changes in primary hepatocytes isolated from livers of *Ptprk*$^{-/-}$ and *Ptprk*$^{+/+}$ mice. **a** Methodological approach for isolation of low/high fat hepatocytes from mice fed high-fat, high-fructose, high-cholesterol diet (HFHFHCD) for 6 weeks. **b** Immunoblot analysis showing PTPRK and PPARγ expression profiles of hepatocytes with high-fat content. **c** RT-qPCR analysis showing changes in the expression of lipid metabolism-related genes. **d** RNA-Seq heatmap displaying alterations in PPAR pathway-related genes. **e** RNA-Seq KEGG pathway enrichment analysis comparing *Ptprk*$^{+/+}$ and *Ptprk*$^{-/-}$ low-fat vs. high-fat hepatocytes. **f** Total proteome global heatmap showing significantly altered proteins in hepatocytes with high-fat content. **g** Volcano plot illustrating the changes in the total proteomic profile between *Ptprk*$^{-/-}$ and *Ptprk*$^{+/+}$ high-fat hepatocytes. **h** Total proteome KEGG pathway enrichment analysis. **i** Phosphoproteome global heatmap showing significantly altered phosphoproteins. **j** Phosphoproteome KEGG pathway enrichment analysis. **k** Volcano plot showing quantification of tyrosine phosphosites in *Ptprk*$^{-/-}$ and *Ptprk*$^{+/+}$ hepatocytes. Phosphosites with over 30% increase in *Ptprk*$^{-/-}$ cells are indicated in red ($p < 0.05$). **l** Heatmap showing phosphopeptides of fructose-1,6-bisphosphatase 1 (F16P1/FBP1) in high-fat hepatocytes. **m** Schematic representation of different F16P1/FBP1 amino acid sequences, indicating distinct boxes for interaction mapping experiments. The predicted helical regions are showed in the three-dimensional structure on the right side. **n** Predicted PTPRK-FBP1 interface illustrating the PTPRK-D2 complex (red-blue-gray surface representation of their electrostatic surface potential) interacting with the FBP1 dimer (light green-red), and the proximity of the PTPRK catalytic site with FBP1 phosphotyrosine residues. **o** Immunoblot analysis of pervanadate-treated mouse hepatocyte lysates incubated with or without the recombinant PTPRK-ICD (ICD: intracellular domain). **p** HYlight-mediated monitoring of fructose 1,6-bisphosphate dynamics in primary mouse hepatocytes. Solid lines represent the mean across cells, while dots represent the mean ± SEM. Scale bar = 50 µm. In **b**, **c**, **p** results are shown as means ± SEM. Statistical analyses were done using two-tailed unpaired Student's *t* test (**b**, **p**), two-way ANOVA (**c**), *p* value adjusted with Benjamini–Hochberg method (**e**), Welch's two-sided *t*-test (**g**), modified Fisher Exact *p* value (**h**, **j**), and Welch's two-sided *t*-test (permutation-based FDR method with 250 randomizations, **k**). Statistical significance in **b**, **c**, **p** is indicated as $^{*}p < 0.05$, $^{**}p < 0.01$, $^{***}p < 0.001$. Source data are provided as a Source Data file.

spectral files and searched the Homo sapiens Uniprot database with false discovery rate (FDR) restricted to 1% at the peptide level. Spectral counting was used to compare the relative abundance among different PTPs, considering that peptides containing the conserved catalytic motif are at least 50% identical in sequence, minimizing potential variability in ionization efficiency.

Mice

Animals were housed at 22 °C on a 12:12-h light-dark cycle with ad libitum access to food and water. *Ptprk* knockout mice were generated at The Jackson Laboratory (Ptprk-8356J-M669 project) by CRISPR/Cas9 technology and were bred on a pure C57BL/6N background. The strategy involved an intragenic deletion spanning 555 base pairs on Chromosome 10. This genetic alteration led to the excision of exon 3 within the *Ptprk* gene, accompanied by the removal of 283 base pairs from adjacent intronic sequences. The resulting mutation is predicted to induce an alteration in the amino acid sequence following residue 74 and an early truncation by 2 amino acids.

By breeding *Ptprk*$^{+/-}$ mice we obtained *Ptprk*$^{-/-}$ and *Ptprk*$^{+/+}$ males and females littermates. *Ptprk*$^{+/+}$ and *Ptprk*$^{-/-}$ mice aged 8 weeks, were randomly assigned to experimental diet-induced obesity feeding with unrestricted access to the specific diets: a HFD (60 kcal% fat D12492), a HFHFHCD (40 kcal% Fat, 20 kcal% Fructose, and 2% Cholesterol, D09100310i), or a control diet (10 kcal% Fat, D09100304i) from Research Diets (New Brunswick, NJ, USA). For the maintenance of the mice and for experiments that did not involve diet-induced obesity, a standard chow diet was employed (RM1 (P) 801151, Special Diets Services, UK). The duration for which the animals were subjected to the experimental diets ranged from 4 to 40 weeks, as indicated. Mice underwent a 6 h fast starting at 9 a.m., with individual housing in cages with clean bedding. The data are reported for males and/or females mice. Liver samples were consistently collected from the center of the left lobe.

Metabolic analysis

Evaluation of body and liver lean and fat mass was performed with EchoMRI™ 3-in-1 (NMR) body composition analyzer from EchoMedical Systems (Houston, TX, USA).

Glucose tolerance tests were performed in 6 h fasted mice with an intraperitoneal administration of glucose (2 g D-Glucose/kg body weight). For pyruvate tolerance tests, mice were fasted overnight and administered pyruvate (2 g/kg). Insulin tolerance tests were performed on mice fasted for 4 h, with an intraperitoneal injection of insulin (0.75U/kg body weight). Fresh D-glucose, pyruvate, or insulin solutions were prepared in PBS immediately before the injections. Blood samples were obtained from the tail tip, and glycemia was measured using a glucometer (Accu-Check Performa, Roche, Basel, Switzerland). Blood serum was collected in a fed state (9 a.m.) or 6 h after fasting (3 p.m.) and insulin levels measured by ELISA (Crystal Chem Inc.).

At 18 weeks of age, *Ptprk*$^{-/-}$ and *Ptprk*$^{+/+}$ mice fed HFHFHCD for 10 weeks, were placed in metabolic cages TSE Phenomaster setup (TSE, Germany) for a duration of 72 h. Following a 24 h period of acclimatization, metabolic parameters, including physical activity, energy expenditure, and substrate utilization were assessed by indirect calorimetry.

DEN-induced HCC

Liver tumor formation was induced by administering 25 mg/kg of DEN in PBS via intraperitoneal injection into the underbelly region of 14-day-old mice. Mice were maintained on a chow diet or a HFHFHCD starting at 6 weeks of age. At the endpoint, the mice were euthanized via cervical dislocation, and livers were collected for comprehensive analysis, including macroscopic and histological assessment of tumor number and size.

Histological analysis

Mouse liver tissues intended for histological analysis were collected from euthanized mice, dissected, and subsequently rinsed with PBS. The tissues were fixed in 4% buffered formaldehyde (pH 7.4), embedded in paraffin blocks, sectioned into slices measuring 5–7 µm using a Leica rotator microtome and stained with haematoxylin and eosin.

For immunohistochemistry analysis of PTPRK in human liver samples, 7 µm thick paraffin sections were situated on positively charged slides. Antigen unmasking was performed with a heated citrate buffer (10 mM, pH 6.0). The sections were permeabilized using triton (0.1%), subsequently blocked with 2% milk, and incubated with 10% normal goat serum to prevent nonspecific binding. Primary antibodies were incubated overnight at 4 °C, followed by incubation with goat anti-rabbit horseradish peroxidase secondary antibody (P044801). Negative controls were established by subjecting specimen slices solely to the secondary antibody.

Hepatic lipid content was assessed in frozen sections of both *Ptprk*$^{+/+}$ and *Ptprk*$^{-/-}$ livers through Oil Red O (ORO) (Sigma-Aldrich, O1391) staining. Liver sections from cryostat cuts were equilibrated for 30 min at room temperature in laminar flow hood. ORO working solution (0.3% ORO in 60% isopropanol) was applied to ensure complete coverage and incubated at 37 °C. After counterstaining with haematoxylin, images were captured using NanoZoomer Digital Pathology (Hamamatsu Photonics K.K., version SQ 1.0.9) at ×40 magnification.

https://doi.org/10.1038/s41467-024-53733-0

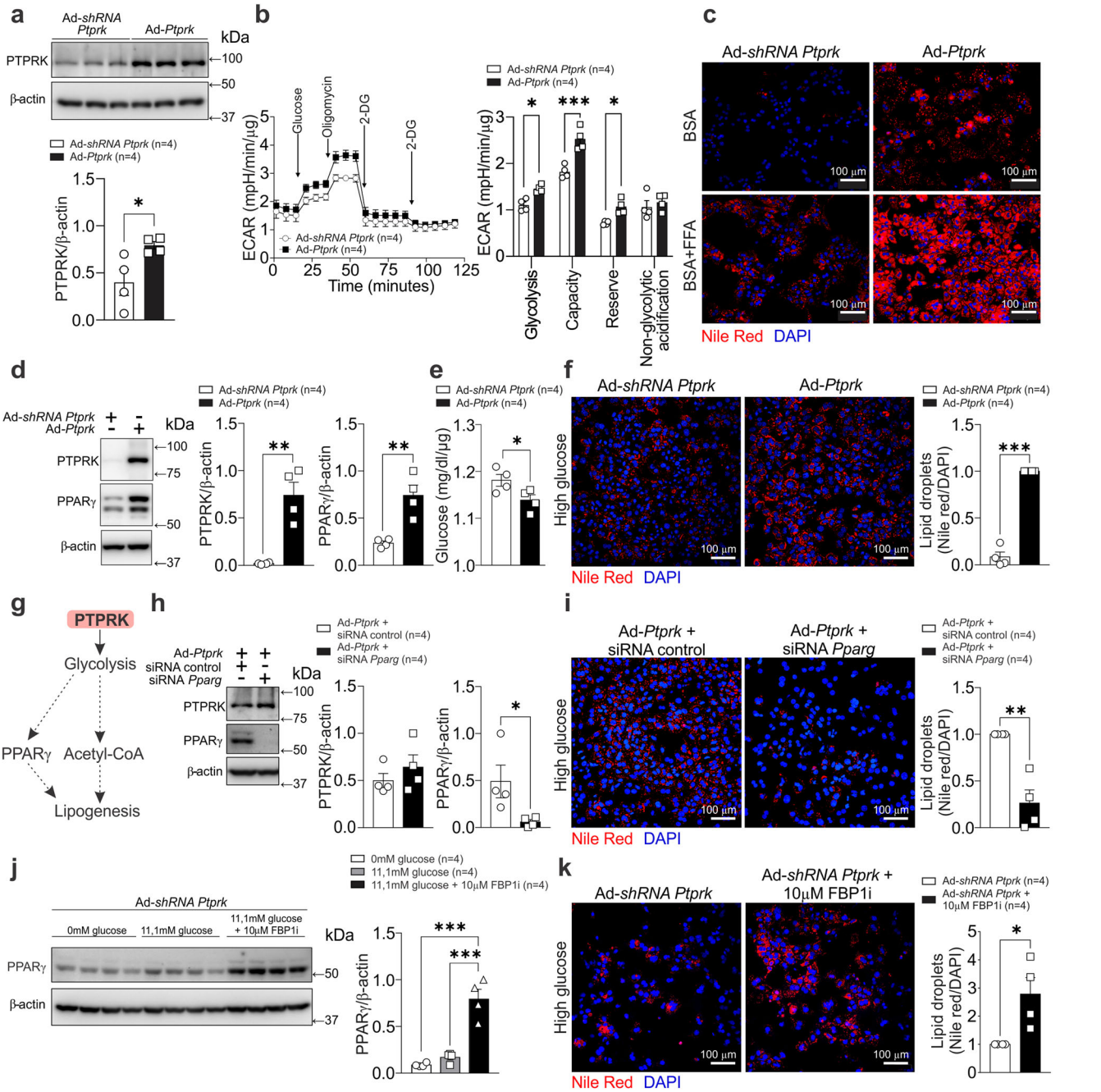

Fig. 6 | PTPRK overexpression enhances glycolysis and PPARγ-dependent lipid accumulation in primary mouse hepatocytes. a Primary mouse hepatocytes were cultured and transduced with an adenoviral vector to induce PTPRK overexpression (Ad-*Ptprk*) or PTPRK silencing (Ad-*shRNA Ptprk*). Immunoblotting confirmed the modulation of PTPRK expression. **b** Real-time measurement of the extracellular acidification rate (ECAR) in response to glycolytic modulators revealed changes in glycolytic parameters. **c** Primary mouse hepatocytes were treated with a mixture of BSA-conjugated fatty acids, palmitate (PA), and oleate (OA) (0.4 mM PA and 0.8 mM OA) for 24 h to simulate triglyceride deposition, followed by Nile Red staining to visualize lipid droplets rich in neutral lipids (triglycerides). Scale bar = 100 μm. **d** Adenoviral-mediated PTPRK overexpression or knockdown in primary mouse hepatocytes was performed followed by exposure to medium containing high concentration (23.5 mM) of glucose. Immunoblot analysis showing PTPRK and PPARγ protein levels. **e** Glucose levels in the medium measured after 48 h and normalized by protein content. **f** The cells were fixed and stained with Nile red to show lipid droplet abundance. Scale bar = 100 μm. **g** Schematic representation of the postulated PTPRK mechanism in hepatocytes, illustrating its role in modulating glycolytic activity, PPARγ and lipid metabolism. **h** Primary mouse hepatocytes overexpressing PTPRK were transfected with siRNA targeting PPARγ or control siRNA and cultured with high glucose (23.5 mM) for 24 h. Immunoblot showing transfection efficiency. **i** Nile red staining was performed to assess lipid droplet accumulation. Scale bar = 100 μm. **j** Primary mouse hepatocytes were transduced with Ad-*shRNA Ptprk* and treated as indicated for 48 h. PPARγ protein levels were measured by immunoblot analysis. **k** Primary mouse hepatocytes were treated with high glucose with or without an FBP1 inhibitor, fixed, and stained with Nile red to visualize lipid droplet abundance. Scale bar = 100 μm. Each individual value represents independent hepatocyte preparations from different mice. In **a**, **b**, **d**–**f**, **h**–**k** results are shown as means ± SEM. Statistical analyses were done using one-way ANOVA (**j**) or two-tailed unpaired Student's *t* test (**a**–**f**, **h**, **i**, **k**). Statistical significance is indicated as $^{*}p < 0.05$, $^{**}p < 0.01$, $^{***}p < 0.001$. Source data are provided as a Source Data file.

https://doi.org/10.1038/s41467-024-53733-0

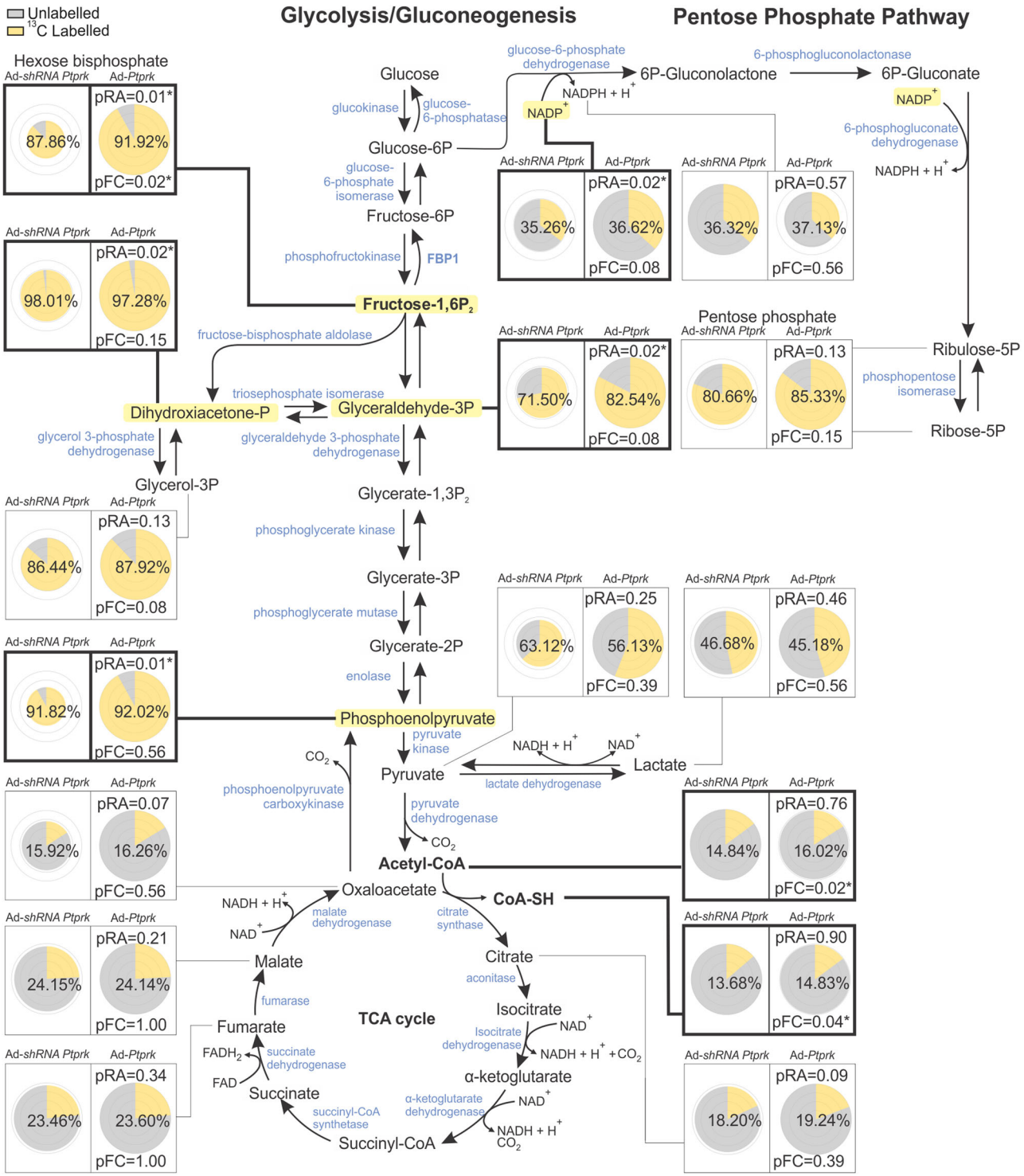

Fig. 7 | Metabolic effects of PTPRK overexpression on glycolytic flux in hepatocytes using $^{13}C_6$-glucose tracing. Primary mouse hepatocytes isolated from individual mice ($n = 4$), were cultured and transduced with an adenoviral vector to induce PTPRK overexpression (Ad-*Ptprk*) or silencing of PTPRK (Ad-*shRNA Ptprk*) and 23.5 mM of $^{13}C_6$ -glucose. Metabolites were extracted and analyzed by MS to quantify isotopologue distributions and contributions, with data corrected for natural abundance and presented as raw abundances normalized to protein content and fractional contributions. Pie chart visualizations by Travis Pies applied to 2 cohorts: Ad-*shRNA Ptprk* and Ad-*Ptprk*. For each metabolite, the pie radii correspond to the relative abundance, which can be compared between the cohorts of this metabolite. The concentric circles correspond from center outwards to 0.25, 0.5, 0.75, and 1 time the largest abundance. Both the labeled surface fraction of the pie and the percentage displayed in the middle of each pie reflect the fractional contribution. pRA and pFC indicate significance of the difference in relative abundance (*t*-test) or fractional contribution (Kruskal–Wallis) with Ad-*shRNA Ptprk* (* indicates a p value < 0.05). Metabolites exhibiting statistically significant changes are highlighted—light yellow for raw abundance (RA) and bold for fractional contribution (FC). Source data are provided as a Source Data file.

https://doi.org/10.1038/s41467-024-53733-0

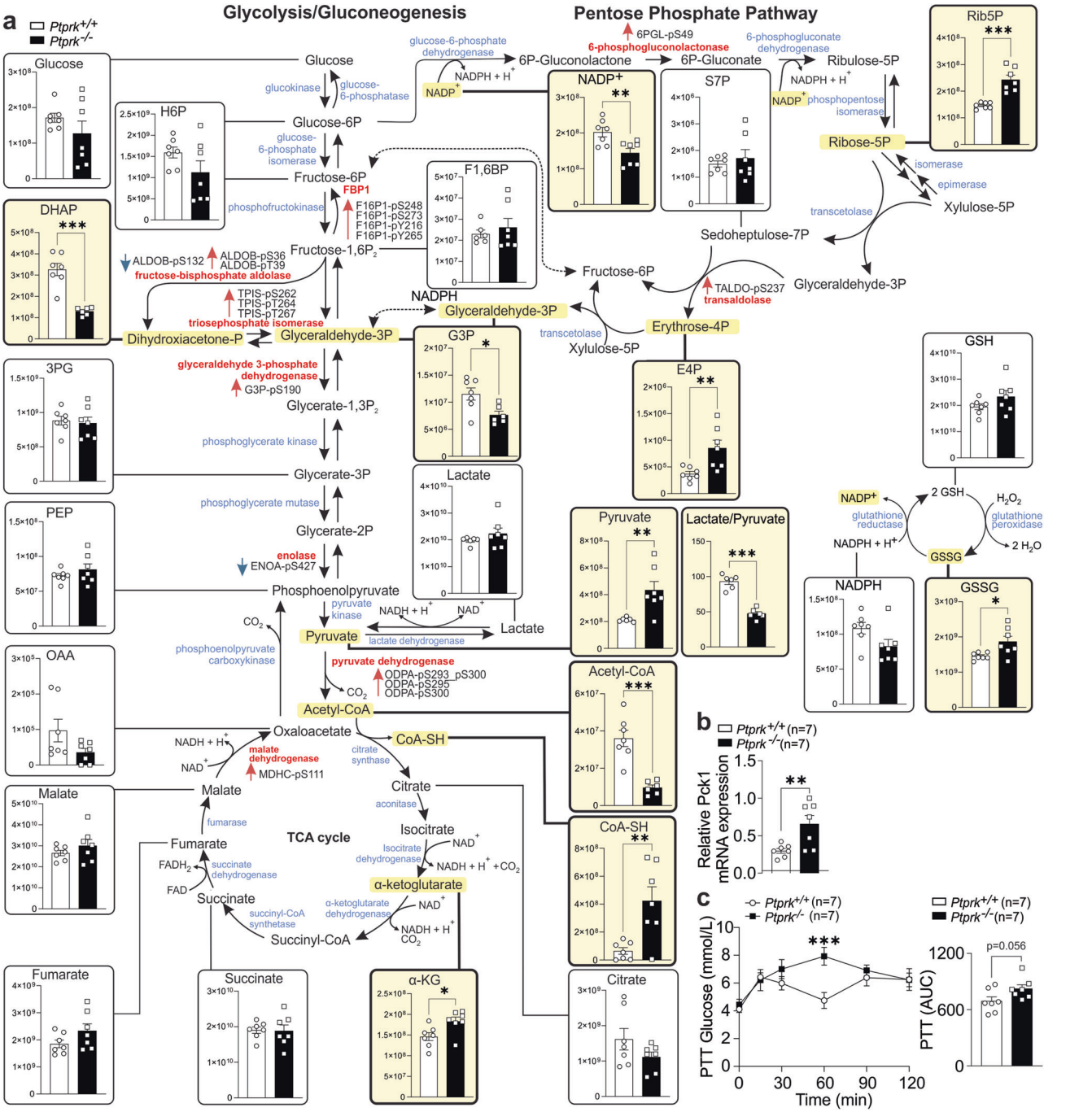

Fig. 8 | Hepatic PTPRK induces metabolic reprogramming in the livers of mice fed an obesogenic diet. a Untargeted metabolomics analysis was conducted in livers from *Ptprk*$^{-/-}$ and *Ptprk*$^{+/+}$ female mice fed high-fat, high-fructose, high-cholesterol diet (HFHFHCD) for 12 weeks. Metabolites exhibiting statistically significant changes are highlighted (light yellow). The data is presented as raw abundances corrected for sample weight. Enzymes associated with these metabolites, which showed significant differences in the levels of phosphorylated amino acid residues based on the analysis presented in Fig. 5i, are indicated in red. Red arrows near highlighted enzymes indicate increased phosphorylation at the indicated amino acid residues, while blue arrows indicate reduced phosphorylation at the indicated amino acid residues. The sample size was $n = 7$ for both *Ptprk*$^{-/-}$ and *Ptprk*$^{+/+}$, except for DHAP, G3P, acetyl-CoA, and the lactate/pyruvate ratio in the *Ptprk*$^{-/-}$ group ($n = 6$) and for pyruvate, lactate, F1,6BP, and the lactate/pyruvate ratio in the *Ptprk*$^{+/+}$ group ($n = 6$). **b** qPCR analysis was performed to assess Pck1 mRNA levels in the livers of *Ptprk*$^{-/-}$ and *Ptprk*$^{+/+}$ mice. **c** Pyruvate tolerance test was conducted in mice fed HFHFHCD for 12 weeks after overnight (16 h) fasting to assess gluconeogenic capacity in response to pyruvate administration. In **a**–**c** results are shown as means ± SEM and statistical analyses were done using two-tailed unpaired Student's *t* test. Statistical significance is indicated as $^{*}p < 0.05$, $^{**}p < 0.01$, $^{***}p < 0.001$. Source data are provided as a Source Data file.

Lipid extraction

Total hepatic lipid content was evaluated by gravimetry after lipid extraction. Livers were removed, immediately freeze-clamped in liquid nitrogen, and stored at −80 °C. The liver samples (100 mg) were homogenized using a bead tissue homogenizer with cold methanol. After sonication, the homogenate was transferred to Falcon tubes. Chloroform was added, and the mixture was vortexed. Following agitation overnight at 4 °C, the samples were centrifuged at 13,500 × *g* for

https://doi.org/10.1038/s41467-024-53733-0

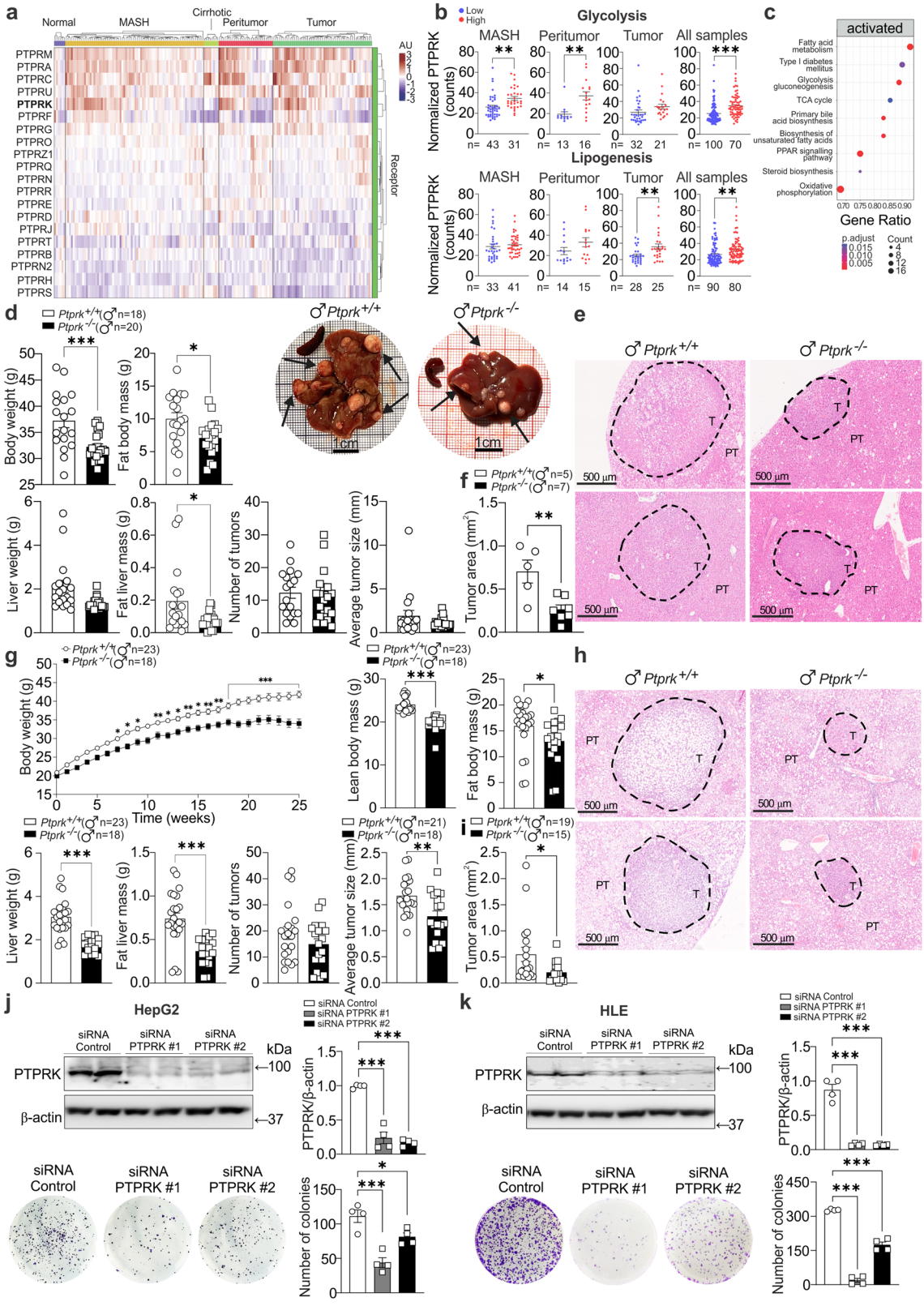

10 min. The organic phase was collected, allowed to air-dry at room temperature, and the resulting pellet was weighed for total fat quantification. The solid middle layer formed during centrifugation was dried and weighed to determine the protein content. The results were expressed as mg of fat/100 g of liver and g of fat/g of protein in the liver.

Primary mouse hepatocyte isolation, cell culture and treatments

Mouse primary hepatocytes were isolated from *Ptprk*$^{-/-}$ and *Ptprk*$^{+/+}$ mice following overnight ad libitum feeding, utilizing a two-step collagenase perfusion method through the vena cava. The process was initiated by anaesthetizing the mice through an intraperitoneal

Fig. 9 | Influence of PTPRK in hepatocellular carcinoma (HCC) development. **a** mRNA expression profiling was conducted on human livers from dataset GSE164760 of normal liver, metabolic dysfunction-associated steatohepatitis (MASH), cirrhotic livers, peritumour regions, and hepatocellular carcinoma (HCC) tumors. **b** Based on the expression levels of PTPRK, samples were categorized as high or low, and the normalized counts of genes involved in glycolysis and lipogenesis were analyzed. **c** KEGG pathway enrichment analysis was performed specifically on tumor samples with low or high PTPRK expression levels. **d**–**i** Male *Ptprk*$^{-/-}$ and *Ptprk*$^{+/+}$ mice were subjected to diethylnitrosamine (DEN) induction of liver cancer at 2 weeks of age. **d**–**f** Mice were fed a chow diet and tumor development was assessed at 40 weeks of age. Body and liver weigh and composition correspond to *Ptprk*$^{-/-}$ ($n = 20$) and *Ptprk*$^{+/+}$ ($n = 18$) mice. **g**–**i** Male *Ptprk*$^{-/-}$ and *Ptprk*$^{+/+}$ mice were fed a high-fat, high-fructose, high-cholesterol diet (HFHFHCD) at 6 weeks of age, and tumor harvesting was performed after 25 weeks of feeding, at 32 weeks of age. Measurements of body weight, fat body mass, liver weight, and fat liver mass were recorded for *Ptprk*$^{-/-}$ ($n = 18$) and *Ptprk*$^{+/+}$ ($n = 23$) mice. Tumors on the surface of the hepatic lobes were counted and measured, considering tumors larger than 0.2 mm. The results are presented as the number of tumors per liver and average tumor size (**d**, **g**). Tumor area measurements were performed using hematoxylin-eosin-stained paraffin-embedded liver sections of the left lobe for the identification and measurement of the area of microtumours within the hepatic lobe. Representative hematoxylin-eosin-stained sections show the presence of nodules, scale bar = 500 µm (**e**, **h**) and tumor area (**f**, **i**). Human hepatoma cell lines HepG2 (**j**) and HLE (**k**) were transfected with siRNAs targeting PTPRK or siRNA control ($n = 4$). Colony-forming capacity was assessed and immunoblot confirmed the knockdown efficiency. In **b**, **d**, **f**, **g**, **i**–**k** results are shown as means ± SEM. Statistical analyses were done using *p* value adjusted with Benjamini–Hochberg method (**c**), two-tailed unpaired Student's *t* test (**b**, **d**, **f**, **g**, **i**), or one-way ANOVA (**j**, **k**). Statistical significance is indicated as $^{*}p < 0.05$, $^{**}p < 0.01$, $^{***}p < 0.001$. Source data are provided as a Source Data file.

injection of a ketamine (100 mg/kg) and xylazine (10 mg/kg) mixture, peritoneum was opened, and the infra-hepatic segment of the vena cava was cannulated for perfusion. The portal vein was cut to clear blood from the liver. In the first perfusion step, the liver was exposed to HBSS (Thermo Fisher Scientific) supplemented with 10 mM HEPES (pH 7.4), saturated with O_2/CO_2 (95:5 vol/vol), at 37 °C for 10 min. The second step involved adding collagenase type IV (0.3 mg/mL) to William's E Medium (Thermo Fisher Scientific) and further perfusing for 10 min, effectively digesting the liver tissue. The digested liver was transferred to a sterile plastic dish, and cells were dispersed using a coarse-toothed comb in cold William's E Medium, followed by filtration through a 100-µm cell filter to eliminate cell clumps. The resulting clump-free cell suspension was pelleted through centrifugation at 50 × *g* for 5 min at 4 °C, the pellet was resuspended in William's E Medium and layered onto Percoll® solution (Sigma-Aldrich) (10 ml Percoll® + 1.25 ml PBS 10X + 1.25 ml H_2O.) The cells were washed with William's E Medium 3 times (centrifugation at 50 × *g* for 5 min at 4 °C). Viability assessment using the trypan blue exclusion test yielded approximately 15–20 million cells with 85% viability. The experimental individual values corresponded to independent hepatocytes preparation from different mice.

Hepatocytes with high-fat and low-fat content were isolated from steatotic livers[40]. Viable hepatocytes with different lipid contents were separated from dead hepatocytes and non-parenchymal cell types in the cell suspension using Percoll® gradient and differential centrifugation. The hepatocytes were resuspended, washed, and assessed for cell number and viability using trypan blue and a hemacytometer and immediately plated for experiments or pelleted and stored at −80 °C for further RNA or protein extractions used in RNA-Seq and proteomic/phosphoproteomic analyses.

HepG2, HLE, and Huh6 cell lines were cultured using DMEM with 10% heat-inactivated FBS and Penicillin-Streptomycin. The authentication of the cell lines was not performed in our laboratory. For mouse primary hepatocytes, 100,000 cells/well in a p24 plate using attachment medium (William's Medium with Glutamax, 10% Fetal Bovine Serum (FBS), 1% Penicillin-Streptomycin, and 10 mM HEPES). After attachment, the media was replaced with a maintenance medium (William's E Medium with Glutamax, 10% FBS, 1% Penicillin-Streptomycin, 1% non-essential amino acids, 10 mM HEPES, and 5 µM hydrocortisone). Cell death was measured using SYTOX green (Thermo Fisher Scientific).

Transfection and imaging of PTPRK-GFP

HepG2 cells were transfected with either full-length PTPRK or the predicted intracellular domain (ICD) of PTPRK (exons 16 to 34, UniProt ID: P35822) fused to mGreenLantern (GFP). The synthesized constructs provided by GenScript were cloned into the pcDNA3.1 plasmid under the control of the CMV IE94 promoter. Confocal microscopy images were captured using a Zeiss LSM780, with excitation wavelengths of 488 nm for mGreenLantern and 405 nm for DAPI.

Adenoviral infection

Adenoviral-mediated hepatic PTPRK overexpression was performed by retro-orbital injection of 1.8×10^9 PFU (Ad-*Ptprk*, construct Ad-m-PTPRK, SKU: ADV-269821) in 200 µL of PBS, and Adv-CMV-Null was used as control (Ad-control, #1300).

In primary mouse hepatocytes, we used adenoviral vectors to achieve PTPRK overexpression (Ad-*Ptprk*, construct Ad-m-PTPRK, SKU: ADV-269821) and silencing (Ad-shRNA *Ptprk*, construct Ad-GFP-U6-m-PTPRK-shRNA, SKU: shADV-269821). The cells were used for the experiments 48 h after the exposure to the vectors. The vectors were obtained from Vector Biolabs.

Lipid accumulation was assessed by Nile Red staining (Sigma-Aldrich N3013). Primary hepatocytes were isolated and seeded onto chambered coverslips (Ibidi) at a density of 50,000 cells per well, 4 h before adenoviral transduction for PTPRK overexpression or silencing. After 24 h of infection, the culture medium was replaced with BSA-conjugated free fatty acids (sodium palmitate 0.4 mM, oleic acid 0.8 mM) or free fatty acid-free 1% BSA control-enriched medium with 1% FBS. Hepatocytes were fixed in 4% formaldehyde solution for 20 min, and stained with a 5 µg/mL Nile Red solution and the nucleus were stained with DAPI. The stained cells were observed using an inverted fluorescence microscope (Axio Observer D1, Carl Zeiss). Fluorescence intensity was measured using NIH ImageJ software based on the mean area of each channel (Nile Red and DAPI). The same staining procedure was applied to primary hepatocytes with high- and low-fat content, fixed, and stained following an overnight culture period.

LC-MS analysis of total proteome and phosphoproteome changes

The cell pellets originating from primary hepatocytes were lysed in cold HEN Buffer supplemented with PhosSTOP (Roche) and cOmplete™, EDTA-free Protease Inhibitor Cocktail (Roche). Lysates were precipitated twice using methanol/chloroform precipitation (Sample:Methanol:Chloroform, 4:4:1). Pellets were resuspended using 2% SDS in 50 mM HEPES, and protein concentration was performed using DC protein assay (Bio-Rad Laboratories). An equal amount of protein was subjected to reduction and alkylation by incubating the samples with 5 mM DTT for 1 h at 37 °C, followed by incubation with 20 mM iodoacetamide at room temperature for 30 min. Pellets were dissolved using 6 M Guanidine-HCl in digestion buffer (50 mM ammonium bicarbonate, 1 mM $CaCl_2$). A total of 250 µg of proteins were diluted to 0.3 M Guanidine-HCl in digestion buffer and digested using trypsin (protein:trypsin, 20:1, w/w). Peptides were desalted on Supel™-Select HLB SPE Tube (Sigma-Aldrich). Eluates were evaporated under a

vacuum until dryness. Peptides were dissolved in 80% acetonitrile and 0.1% TFA. Before enrichment, digestion quality control was performed using an Ultimate 3000 Nano Ultra High-Pressure Chromatography system with a PepSwift Monolithic® Trap 200 μm*5 mm (Thermo Fisher Scientific). One part of the sample was kept aside and dried again for total proteomic analysis. The phosphorylated peptides enrichment was performed using Fe(III)-NTAcartridges (Agilent Technologies) using the AssayMAP Bravo Platform (Agilent Technologies)[41]. Cartridges were primed and equilibrated with 0.1% TFA in ACN and 0.1% TFA, 80% ACN (loading buffer) solutions, respectively. Cartridges were then washed with loading buffer and eluted using 1% NH_4OH. Peptides were immediately acidified using 10% formic acid (FA) and dried in vacuum. Both total proteome and phosphoproteome were analyzed by high-resolution LC-MS/MS using an Ultimate 3000 Nano Ultra High-Pressure Chromatography system (Thermo Fisher Scientific) coupled with an Orbitrap Eclipse™ Tribrid™ Mass Spectrometer via an EASY-spray (Thermo Fisher Scientific). For the total proteome analysis, peptide separation was carried out with an Acclaim™ PepMap™ 100 C18 column (Thermo Fisher Scientific) using a 155 min linear gradient from 3 to 35% of B (84% ACN, 0.1% FA) at a flow rate of 250 nL/min. The peptide separation for the phosphoproteome analysis was carried out with an Acclaim™ PepMap™ 100 C18 column (Thermo Fisher Scientific) using a 155 min non-linear gradient from 3 to 35% of B (0 min, 3% B; 135 min, 30% B; 155 min, 42% B; B: 84% ACN, 0.1% FA) at a flow rate of 250 nL/min. Both were analyzed using the Orbitrap Eclipse™ operated in a DDA mode. MS1 survey scans were acquired from 300 to 1500 m/z at a resolution 120,000 using the Orbitrap mode. MS2 scans were carried with high-energy collision-induced dissociation (HCD) at 32% using the Normal speed IonTrap mode. Data were evaluated with Proteome Discoverer software using 10 ppm for precursor mass tolerance, 0.5 Da for the fragment mass tolerance, specific tryptic digest, and a maximum of 3 missed cleavages. For all datasets, the search was performed against the UniProt mouse database (UP000000589). Carbamidomethylation (+57.021464 Da) on C was added as a fixed modification. N-term Acetylation (+42.010565 Da) and methionine oxidation (+15.994915 Da) were added as variable modifications. Phosphorylation (+79.966331) on S, T, and Y was added as variable modification only for the phospho-proteome analysis in addition to other mentioned modifications. Peptide-spectrum matches and proteins were filtered at FDR 1%. Protein abundancies (total proteome) were normalized using TIC. Phosphorylated peptide abundancies were normalized using eigenMS[42] with R studio.

LC-MS metabolomics analysis

Metabolomics analyses were performed at the VIB Metabolomics Core (Leuven, Belgium). Primary mouse hepatocytes were transfected with adenoviral vectors for PTPRK silencing or overexpression, and after 24 h of adenoviral transfection the cells were cultured for an additional 48 h in Williams' E Medium (no glucose, no glutamine, Genaxxon bioscience) supplemented with 10% fetal bovine serum and 23.5 mM fully labeled $^{13}C_6$-glucose. The experiment was conducted in quadruplicate with cells isolated from four different mice. Two additional setups using $^{12}C_6$-glucose (one Ad-*Ptprk* and one Ad-shRNA *Ptprk*) served as controls. After treatment, the glucose content in the medium was measured (GlucCell Glucose Monitoring System; Cesco Bioengineering), the medium was removed, and the cells were washed with ice-cold NaCl (150 mM). The washing buffer was removed, and the cells were extracted in 80% methanol (LC–MS grade, VWR, Leuven, Belgium) containing internal standards (3 μM $^{13}C_5$-D_5-^{15}N Glutamic acid, 3 μM D_7-$^{15}N_4$ Arginine, and 5 μM D_7-Glucose). Samples were centrifuged at 4 °C, and the supernatants were transferred to MS vials. For protein pellet analysis, 200 mM NaOH solution was added, the pellets were heated at 95 °C for 30 min to solubilize the proteins, then cooled on ice and centrifuged at 4 °C. The supernatant was used to determine the protein concentration using the BCA assay for normalization.

Ten μl of each sample was loaded into a Dionex UltiMate 3000 LC System (Thermo Scientific Bremen, Germany) equipped with a C-18 column (Acquity UPLC-HSS T3 1.8 μm; 2.1 × 150 mm, Waters) coupled to a Q Exactive Orbitrap mass spectrometer (Thermo Scientific) operating in negative ion mode. The gradient started with 0% solvent B (100% methanol) and 100% solvent A (10 mM TBA and 15 mM acetic acid) and remained at 0% B for 2 min post-injection. A linear gradient to 36.3% B was performed for 7 min and increased to 90.9% for 14 min. Between 14–26 min, the gradient increased to 90.9% B and remained at 90.9% B for 4 min. At 30 min, the gradient returned to 0% B. Chromatography was stopped at 40 min. The flow was kept constant at 0.25 mL/min, and the column was maintained at 40 °C throughout the analysis. The MS operated in full scan mode (*m/z* range: [70.0000–1050.0000]) with a spray voltage of 4.80 kV, capillary temperature of 300 °C, sheath gas at 40.0, and auxiliary gas at 10.0. The AGC target was set at 3.0E + 006 using a resolution of 140,000, with a maximum IT fill time of 512 ms. Data were collected using the Xcalibur software (Thermo Scientific). Data analyses were performed by integrating peak areas (El-Maven—Polly—Elucidata). The abundances were normalized by protein content, and graphs were generated using TraVis Pies[43].

Ten μl of each mouse liver sample were loaded into the same LC-MS system. The gradient started with 5% solvent B and 95% solvent A and remained at 5% B for 2 min post-injection. A linear gradient of 37% B was performed for 7 min and increased to 41% for 14 min. Between 14–26 min, the gradient increased to 95% B and remained at 95% B for 4 min. At 30 min, the gradient returned to 5% B. Chromatography was stopped after 40 min. The flow rate, column temperature, and MS operating conditions were the same as those used in the targeted metabolomics analysis. Data collection and analysis were performed using the same software and methods. The results were normalized by liver weight.

In vitro RNA interference and colony formation assay

To induce PTPRK knockdown, we transfected HepG2, HLE, and Huh6 cells with siRNAs targeting PTPRK or a negative control siRNA (working concentration 30 nM; QIAGEN). To induce PPARγ knockdown, we transfected primary mouse hepatocytes with siRNAs targeting *Pparg* or a negative control siRNA 24 h after adenoviral transfection. The delivery of siRNA was achieved using Lipofectamine™ RNAiMAX Transfection Reagent (Thermo Fisher Scientific) in Opti-MEM™ I Reduced Serum Medium (Thermo Fisher Scientific). The siRNA target sequences and references are detailed in Supplementary Table 2.

Forty-eight hours after siRNA transfection, the cells were trypsinized to obtain single-cell suspension. For colony formation assays, 2000 cells were seeded into P6 plates. After 1–2 weeks, depending on the specific cell line, the resultant colonies were fixed with 4% PFA solution and stained with 0.5% crystal violet.

Twenty-four hours after siRNA transfection in primary hepatocytes, cells were treated with William's E Medium supplemented with 10% FBS for an additional 24 h before being harvested for immunoblot analysis or fixed for Nile red staining.

Extracellular acidification rates measurement during glycolytic stress test

Glycolytic rates were evaluated using the XFp Flux Analyzer from Seahorse Bioscience (Agilent Technologies). Primary hepatocytes were plated in the Seahorse plates (10,000 cells/well). After attachment and adenoviral treatments, the cells were allowed to equilibrate in XF Base media (glucose-free, Seahorse Bioscience) supplemented with 2 mM glutamine at 37 °C for 1 h in a CO_2-depleted incubator. The XF Base media was refreshed again immediately before starting the ECAR measurements. The glycolytic stress test was conducted adding glucose (10 mM), oligomycin (10 μM), and 2-DG (100 mM, divided into two consecutive injections of 50 mM). After the test, the medium was removed, and the cells were immediately collected in 50 μl of cell lysis

buffer (Cell Signaling Technology) supplemented with Halt protease and phosphatase inhibitor cocktail (Thermo Fisher Scientific). The cells were stored at −80 °C for posterior protein measurements and immunoblot analysis.

Measurement of fructose 1,6-bisphosphate in cells using HYlight

The HYlight biosensor[22] responds to changes in fructose 1,6-bisphosphate levels. Cells were transfected with the pCS2 + _HYlight plasmid[22] using Lipofectamine 3000 (Thermo Fisher). One hour before imaging, cells were subjected to glucose starvation using XF assay medium. Live-cell imaging was conducted on a Nikon AX confocal system and a 20X objective (NA 0.8, Plan Apo λD 20x OFN 25 DIC N2) with the perfect focus system (PFS). The transfected cells were excited at 488 nm and 405 nm, and emission was captured using a 525/25 nm emission filter. Imaging was performed at 37 °C. Image processing was performed with NIS-Elements software (Nikon), single-cell regions of interest (ROIs) were manually selected. The excitation ratio $F_{488}/_{405}$ was measured for each ROI over time.

Stem cell differentiation into HLCs

PTPRK wild-type and knockout[44] CRISPR/Cas12-edited hESC H1 (WiCell) were differentiated into HLCs[45]. Laminin-coated plates were prepared and stem cells were detached, seeded into the laminin-coated plates. HLC differentiation started at 60–70% confluence with RPMI 1640 medium, B27, Activin A, and Wnt3a to induce definitive endoderm. The cells were then cultured with a medium containing KO-DMEM, KO-serum, Glutamax, non-essential amino acids, β-mercaptoethanol, and DMSO to induce hepatoblast differentiation. In the final stage, the cells were cultured in HepatoZYME medium supplemented with Glutamax, hepatocyte growth factor, hydrocortisone, and oncostatin M. RPMI 1640, KO-DMEM, B27, Glutamax, and HepatoZYME were obtained from Thermo Fisher Scientific; Activin A, hepatocyte growth factor, and oncostatin M were sourced from PeproTech, Wnt3a was obtained from R&D Systems, and DMSO and hydrocortisone were purchased from Sigma-Aldrich. Albumin was measured in the cell culture medium by Human ALB/Serum albumin ELISA Kit (Sigma-Aldrich) and in the cell lysate by qPCR. The differentiated cells were used for glycolytic stress tests.

Western blotting, immunoprecipitation and dephosphorylation assay

RIPA buffer (Cell Signaling Technology) was used to extract total protein lysates from tissues, while cell total protein lysates were prepared using Cell Lysis Buffer (Cell Signaling Technology). Both lysis buffers were supplemented with Halt protease and phosphatase inhibitor cocktail (Thermo Fisher Scientific). Protein quantification was performed using a BCA protein assay kit (Thermo Fisher Scientific). Separated by polyacrylamide gels, 20–50 μg of protein lysate was subsequently transferred to a 0.22 μM nitrocellulose membrane (Bio-Rad Laboratories). Primary antibodies (Supplementary Table 3) were diluted in milk-blocking buffer. Detection of proteins employed goat anti-rabbit IgG (Dako Agilent), goat anti-mouse IgG (Dako Agilent), and Peroxidase AffiniPure Donkey Anti-Human IgG (Jackson ImmunoResearch) secondary antibodies. Immunoreactive bands were detected using a Western blot imaging system (Amersham ImageQuant 800 Western blot imaging system, Cytiva Life Science).

The dephosphorylation assay employed pTyr-enriched lysates obtained from primary mouse hepatocytes treated with pervanadate[13]. The hepatocytes were incubated with a recombinant PTPRK intracellular domain (PTPRK-ICD, 150 nM final concentration). The reaction was stopped after 90-min using SDS, and the resulting samples were subjected to immunoblot analysis of phospho-FBP1 (pY265).

HepG2 cells were transfected with plasmids containing either human Myc-DDK-tagged FBP1 wild-type or a triple tyrosine mutant (Y265F, Y245F, Y216F) using Lipofectamine 3000 (pCMV6 mammalian promoter). Fifteen μg of purified recombinant His.TEV.Avi.PTPRK ICD D1057A[13] was conjugated to 20 μl of pre-washed Ni-Sepharose His-tagged protein resin at room temperature for 1 h on a rotor. The conjugated resins were washed twice with TBST (0.03%). The washed resins were then incubated with 200 μl of pervanadate-treated[13] HepG2 lysates at room temperature for 1 h on a rotor. The resins were washed five times with TBST (0.02%) supplemented with 20 mM imidazole. The resins were resuspended in 20 μl of 2X SDS-PAGE sample buffer and incubated at 95 °C for 10 min. The elutes were diluted to 1X with 20 μl of water.

HepG2 cells were transduced with an adenoviral vector to induce PTPRK overexpression (Ad-PTPRK) and then transfected with plasmids to express human FBP1-myc wild-type or triple tyrosine mutant (Y216F, Y245F, Y265F). Transfected and pervanadate-treated HepG2 cells were lysed and incubated with anti-Myc magnetic beads at room temperature for 1 h on a rotor. The beads were washed five times with TBST (0.02%). The beads were resuspended in 2X SDS-PAGE sample buffer and incubated at 95 °C for 10 min. The elutes were diluted to 1X with 20 μl of water.

Octet® Bio-Layer Interferometry (BLI)

All proteins were prepared in 50 mM HEPES (pH 7.4, 100 mM NaCl, 0.05% Tween-20). His-tagged human FBP1 (MedChemExpress) and His-tagged MATH domain of USP7 (negative control) were loaded into hydrated Octet Ni2+-NTA sensors at a concentration of 20 ng/μl. The analyte concentration (tag-free PTPRK ICD) was fixed at 200 nM. The His-tagged MATH domain of USP7 (22 kDa) was used as a reference (negative control) to eliminate the PTPRK binding to the biosensor. Background subtraction was performed to remove non-specific binding of PTPRK to the biosensor.

RNA extraction, qPCR, and transcriptomics analysis

Poly(A)+ mRNA extraction was performed with Dynabeads™ mRNA DIRECT™ Purification Kit (Thermo Fisher Scientific). Reverse transcription was carried out with a reverse transcriptase kit (Eurogentec). Quantitative real-time PCR was performed using a Bio-Rad CFX (Bio-Rad Laboratories) and SYBR Green reagents (Bio-Rad Laboratories). Probe and primer details can be found in Supplementary Table 4. For tissues or isolated hepatocytes with high-fat and low-fat content the total RNA was obtained using a RNeasy Mini Kit (QIAGEN) following the manufacturer's instructions. cDNA synthesis and qPCR were performed as described above. For the transcriptomics experiments, total RNA quality analysis, library preparation, and sequencing were performed by the BRIGHTcore facility (Brussels, Belgium). Sequencing was performed on an Illumina NovaSeq 600. An average of 25 million paired-end reads of 100 nucleotides were obtained per sample. The list of up-/downregulated genes/transcripts and association with canonical pathways were determined with the use of the online Degust software with Limma/Voom and packages Bioconductor EGSEA and ComplexHeatmap in RStudio.

Bioinformatic analysis

For the comparative analysis among healthy, steatosis and MASH conditions, the Kruskal–Wallis test was employed. The comparison analysis was conducted on mRNA expression data from the publicly available E-MEXP-3291 study, and the analysis was executed using R (version 4.2.2). The correlation analysis focused on investigating the relationship between Ppar mRNA (x-axis) and RPTPs mRNA (y-axis) using the Pearson correlation method. The data was obtained from the publicly available E-GEOD-48452 study. The analysis was performed in R (version R 4.2.2). To assess the statistical significance of the correlation, a significance level ($p < 0.05$) was set, and p values were calculated. To study the expression of RPTPs in human liver, single-cell RNA-Seq dataset of human healthy-obese livers was obtained from ref. 18. The dataset along with cell annotations were downloaded from Gene

Expression Omnibus (GEO), accession number GSE192740. Using the information provided by the authors, the UMAP and gene expression were plotted using Seurat[46]. Publicly available transcriptomic data (RNA-seq) corresponding to GSE164760 was downloaded from the NCBI Sequence Read Archive (SRA) in fastq format using version 3.0.0 of the *SRA Toolkit*. Adapter sequences were removed using *TrimGalore* version 0.6.0 with *Cutadapt* version 1.18[47]. The clean reads were aligned to the reference genome using the splice-aware aligner *STAR* version 020201[48] based on the hg38 genome version. The aligned reads were quantified using *HTseq* version 0.11.0. The trimmed mean of M values method was used with *EdgeR*version 3.28.1[49], R software (version 3.6.3).

Heatmap visualization was carried out with *ComplexHeatmap* R package and all samples were referred to the mean of the control groups, $\log_2$ transformed with trimmed standard deviation in proteomic and transcriptomic databases.

Statistical analysis

The *n* was calculated per individual sample or mouse, independent hepatocyte preparation, or independent experiment. The results are presented as the mean ± standard error of the mean (SEM). Student's *t* test was used for comparisons between two groups. Differences among groups were assessed by two-way ANOVA or repeated-measures ANOVA. Statistical analyses were assessed using Prism software (GraphPad Software, Inc, La Jolla, CA, USA). Sample size was predetermined based on the variability observed in prior experiments and on preliminary data. Differences were regarded as statistically significant if $^{*}p < 0.05$; $^{**}p < 0.01$; $^{***}p < 0.001$.

Reporting summary

Further information on research design is available in the Nature Portfolio Reporting Summary linked to this article.

Data availability

All data needed to evaluate the conclusions are present in the paper, Supplementary Materials, Source Data files or publicly available repositories. The datasets GSE192740, E-MEXP-3291, E-GEOD-48452, and GSE164760 have been used for the study. The RNA-Seq dataset generated during the sequencing procedure is deposited in the Gene Expression Omnibus database (access number GSE247670), the mass spectrometry proteomics and peptidomics datasets have been deposited to the ProteomeXchange Consortium via the PRIDE partner repository (access numbers PXD046940, PXD046506) and available from the corresponding author upon request. Source data are provided with this paper.

References

1. Rinella, M. E. et al. A multi-society Delphi consensus statement on new fatty liver disease nomenclature. *Hepatology* https://doi.org/10.1097/HEP.0000000000000520 (2023).
2. Devarbhavi, H. et al. Global burden of liver disease: 2023 update. *J. Hepatol.* **79**, 516–537 (2023).
3. Brahma, M. K. et al. Oxidative stress in obesity-associated hepatocellular carcinoma: sources, signaling and therapeutic challenges. *Oncogene* **40**, 5155–5167 (2021).
4. Talamantes, S. et al. Non-alcoholic fatty liver disease and diabetes mellitus as growing aetiologies of hepatocellular carcinoma. *JHEP Rep.* **5**, 100811 (2023).
5. Huang, D. Q. et al. Hepatocellular carcinoma surveillance—utilization, barriers and the impact of changing aetiology. *Nat. Rev. Gastroenterol. Hepatol.* https://doi.org/10.1038/s41575-023-00818-8 (2023).
6. Gurzov, E. N., Stanley, W. J., Brodnicki, T. C. & Thomas, H. E. Protein tyrosine phosphatases: molecular switches in metabolism and diabetes. *Trends Endocrinol. Metab.* **26**, 30–39 (2015).
7. Tonks, N. K. Protein tyrosine phosphatases-from housekeeping enzymes to master regulators of signal transduction. *FEBS J.* **280**, 346–378 (2013).
8. Li, S. et al. Cytoplasmic tyrosine phosphatase Shp2 coordinates hepatic regulation of bile acid and FGF15/19 signaling to repress bile acid synthesis. *Cell Metab.* **20**, 320–332 (2014).
9. Grohmann, M. et al. Obesity drives STAT-1-dependent NASH and STAT-3-dependent HCC. *Cell* **175**, 1289–1306.e1220 (2018).
10. Gurzov, E. N. et al. Hepatic oxidative stress promotes insulin-STAT-5 signaling and obesity by inactivating protein tyrosine phosphatase N2. *Cell Metab.* **20**, 85–102 (2014).
11. Young, K. A., Biggins, L. & Sharpe, H. J. Protein tyrosine phosphatases in cell adhesion. *Biochem. J.* **478**, 1061–1083 (2021).
12. Brenachot, X. et al. Hepatic protein tyrosine phosphatase receptor gamma links obesity-induced inflammation to insulin resistance. *Nat. Commun.* **8**, 1820 (2017).
13. Fearnley, G. W. et al. The homophilic receptor PTPRK selectively dephosphorylates multiple junctional regulators to promote cell-cell adhesion. *Elife* **8**, https://doi.org/10.7554/eLife.44597 (2019).
14. Trynka, G. et al. Dense genotyping identifies and localizes multiple common and rare variant association signals in celiac disease. *Nat. Genet.* **43**, 1193–1201 (2011).
15. Inshaw, J. R. J., Walker, N. M., Wallace, C., Bottolo, L. & Todd, J. A. The chromosome 6q22.33 region is associated with age at diagnosis of type 1 diabetes and disease risk in those diagnosed under 5 years of age. *Diabetologia* **61**, 147–157 (2018).
16. Anders, L. et al. Furin-, ADAM 10-, and gamma-secretase-mediated cleavage of a receptor tyrosine phosphatase and regulation of beta-catenin's transcriptional activity. *Mol. Cell Biol.* **26**, 3917–3934 (2006).
17. Xu, Y., Xue, S., Zhou, J., Voorhees, J. J. & Fisher, G. J. Notch and TGF-beta pathways cooperatively regulate receptor protein tyrosine phosphatase-kappa (PTPRK) gene expression in human primary keratinocytes. *Mol. Biol. Cell* **26**, 1199–1206 (2015).
18. Guilliams, M. et al. Spatial proteogenomics reveals distinct and evolutionarily conserved hepatic macrophage niches. *Cell* **185**, 379–396.e338 (2022).
19. Barclay, J. L. et al. GH-dependent STAT5 signaling plays an important role in hepatic lipid metabolism. *Endocrinology* **152**, 181–192 (2011).
20. Hasenfuss, S. C. et al. Regulation of steatohepatitis and PPARgamma signaling by distinct AP-1 dimers. *Cell Metab.* **19**, 84–95 (2014).
21. Li, F. et al. FBP1 loss disrupts liver metabolism and promotes tumorigenesis through a hepatic stellate cell senescence secretome. *Nat. Cell Biol.* **22**, 728–739 (2020).
22. Koberstein, J. N. et al. Monitoring glycolytic dynamics in single cells using a fluorescent biosensor for fructose 1,6-bisphosphate. *Proc. Natl Acad. Sci. USA* **119**, e2204407119 (2022).
23. Valenti, L. et al. Hepatic notch signaling correlates with insulin resistance and nonalcoholic fatty liver disease. *Diabetes* **62**, 4052–4062 (2013).
24. Regnier, M., Carbinatti, T., Parlati, L., Benhamed, F. & Postic, C. The role of ChREBP in carbohydrate sensing and NAFLD development. *Nat. Rev. Endocrinol.* **19**, 336–349 (2023).
25. Yang, F. et al. Metabolic reprogramming and its clinical implication for liver cancer. *Hepatology* https://doi.org/10.1097/HEP.0000000000000005 (2023).
26. Guertin, D. A. & Wellen, K. E. Acetyl-CoA metabolism in cancer. *Nat. Rev. Cancer* **23**, 156–172 (2023).
27. Luo, X. et al. The fatty acid receptor CD36 promotes HCC progression through activating Src/PI3K/AKT axis-dependent aerobic glycolysis. *Cell Death Dis.* **12**, 328 (2021).

28. Broadfield, L. A. et al. Fat induces glucose metabolism in non-transformed liver cells and promotes liver tumorigenesis. *Cancer Res.* **81**, 1988–2001 (2021).
29. Martinez-Reyes, I. & Chandel, N. S. Mitochondrial TCA cycle metabolites control physiology and disease. *Nat. Commun.* **11**, 102 (2020).
30. Stine, Z. E., Schug, Z. T., Salvino, J. M. & Dang, C. V. Targeting cancer metabolism in the era of precision oncology. *Nat. Rev. Drug Discov.* **21**, 141–162 (2022).
31. Chen, Y. W. et al. Receptor-type tyrosine-protein phosphatase kappa directly targets STAT3 activation for tumor suppression in nasal NK/T-cell lymphoma. *Blood* **125**, 1589–1600 (2015).
32. Yuan, Y. et al. alpha-Ketoglutaric acid ameliorates hyperglycemia in diabetes by inhibiting hepatic gluconeogenesis via serpina1e signaling. *Sci. Adv.* **8**, eabn2879 (2022).
33. Morris, J. P. et al. alpha-Ketoglutarate links p53 to cell fate during tumour suppression. *Nature* **573**, 595–599 (2019).
34. Brownstein, A. J., Veliova, M., Acin-Perez, R., Liesa, M. & Shirihai, O. S. ATP-consuming futile cycles as energy dissipating mechanisms to counteract obesity. *Rev. Endocr. Metab. Disord.* **23**, 121–131 (2022).
35. Stanford, S. M. & Bottini, N. Targeting protein phosphatases in cancer immunotherapy and autoimmune disorders. *Nat. Rev. Drug Discov.* **22**, 273–294 (2023).
36. Liang, S. et al. A small molecule inhibitor of PTP1B and PTPN2 enhances T cell anti-tumor immunity. *Nat. Commun.* **14**, 4524 (2023).
37. Baumgartner, C. K. et al. The PTPN2/PTPN1 inhibitor ABBV-CLS-484 unleashes potent anti-tumour immunity. *Nature* https://doi.org/10.1038/s41586-023-06575-7 (2023).
38. Qian, Z. et al. Manipulating PTPRD function with ectodomain antibodies. *Genes Dev.* **37**, 743–759 (2023).
39. Powell, E. E., Wong, V. W. & Rinella, M. Non-alcoholic fatty liver disease. *Lancet* **397**, 2212–2224 (2021).
40. Jung, Y., Zhao, M. & Svensson, K. J. Isolation, culture, and functional analysis of hepatocytes from mice with fatty liver disease. *STAR Protoc.* **1**, 100222 (2020).
41. Post, H. et al. Robust, sensitive, and automated phosphopeptide enrichment optimized for low sample amounts applied to primary hippocampal neurons. *J. Proteome Res.* **16**, 728–737 (2017).
42. Karpievitch, Y. V. et al. Normalization of peak intensities in bottom-up MS-based proteomics using singular value decomposition. *Bioinformatics* **25**, 2573–2580 (2009).
43. De Craemer, S., Driesen, K. & Ghesquiere, B. TraVis Pies: a guide for stable isotope metabolomics interpretation using an intuitive visualization. *Metabolites* **12**, https://doi.org/10.3390/metabo12070593 (2022).
44. Negueruela, J. et al. Protocol for CRISPR-Cas12a genome editing of protein tyrosine phosphatases in human pluripotent stem cells and functional beta-like cell generation. *STAR Protoc.* **5**, 103297 (2024).
45. Wang, Y. et al. Defined and scalable generation of hepatocyte-like cells from human pluripotent stem cells. *J. Vis. Exp.* https://doi.org/10.3791/55355 (2017).
46. Hao, Y. et al. Dictionary learning for integrative, multimodal and scalable single-cell analysis. *Nat. Biotechnol.* https://doi.org/10.1038/s41587-023-01767-y (2023).
47. Kechin, A., Boyarskikh, U., Kel, A. & Filipenko, M. cutPrimers: a new tool for accurate cutting of primers from reads of targeted next generation sequencing. *J. Comput. Biol.* **24**, 1138–1143 (2017).
48. Dobin, A. et al. STAR: ultrafast universal RNA-seq aligner. *Bioinformatics* **29**, 15–21 (2013).
49. Robinson, M. D., McCarthy, D. J. & Smyth, G. K. edgeR: a Bioconductor package for differential expression analysis of digital gene expression data. *Bioinformatics* **26**, 139–140 (2010).

Acknowledgements

We thank André Dias, Madalina Popa, Erick Arroba, Mariana Nunes, Francisco Costa, Anne Van Praet and Anaïs Schaschkow (Université Libre de Bruxelles) for experimental and technical support, Nicolas Baeyens (Université Libre de Bruxelles) for live-imaging microscopy advice, Laurine Verset and Flavienne Sandras (HUB pathology department) for human liver samples, John Koberstein (Howard Hughes Medical Institute) for the HYlight biosensor, Carlos Martinez-Cáceres (IMIB) for pathological analysis of the samples, the Consortium des Équipements de Calcul Intensif (CÉCI) for the computer cluster NIC5, and Hercules2 for providing computing facilities. We thank Cédric Blanpain (Université Libre de Bruxelles), Sarah-Maria Fendt (KULeuven) and Latifa Bakiri (Medical University of Vienna) for critical reading of the manuscript. This work was supported by a European Research Council (ERC) Consolidator grant METAPTPs (Grant Agreement No. GA817940), FNRS-WELBIO grant (35112672), FNRS-PDR grant (40007740), FNRS-TELEVIE grants (40007402, 40025595), and ULB Foundation. The Ministry of Science and Innovation, through its State Plan for Scientific, Technical and Innovation Research (Project PID2021-125188OB-C32) and the Generalitat Valenciana (PROMETEO/2021/059) supported the work in the Encinar laboratory. M.R.F. is funded by European Research Council (ERC) under the European Union's Horizon 2020 research and innovation programme (Grant Agreement No. 864921). J.M. is supported by a VIB grant. H.J.S. is supported by a fellowship jointly funded by Wellcome Trust and Royal Society: 109407/A/15/A, and a Biotechnology and Biological Sciences Research Council institutional programme grant [BBS/E/B/000C0433]. W.W. is supported by Singapore Immunology Network (SIgN), Agency for Science, Technology and Research (A*STAR); Biomedical Research Council (BMRC) Core Research Fund for use-inspired basic research (UIBR) and IAF-PP project H22J2a0043, and Singapore National Medical Research Council (NMRC) project MOH-001401-00. E.N.G. is a Research Associate of the FNRS, Belgium.

Author contributions

E.N.G. was responsible for the conceptualization and design of the study. E.H.G. was responsible for the design and execution of most of the experiments. A.L., W.S.-W., T.-K.S., I.P.-C., G.H., M.L., J.N., and S.D. performed experiments. V.V., J.M.H., Z.F., and S.P.S. performed bioinformatic analyses. J.B.-M., T.V., M.R.F., and W.W. designed and performed proteomic analyses. L.O.S., J.D., and E.T. provided human liver samples, patient characterization and data analysis. F.L. and A.P. were responsible for the initiation of the study. D.E., H.J.S., and J.M. provided materials and designed the immunoprecipitation and biochemistry experiments. D.C.H. provided the protocol and assistance for the differentiation of hepatocyte-like cells. J.A.E. provided computational modeling. E.N.G. and E.H.G. wrote the manuscript and interpreted the data with intellectual input and approval from all authors.

Competing interests

D.C.H. is a founder, director and shareholder in Stimuliver ApS and Stemnovate Limited. E.H.G., J.A.E. and E.N.G. are inventors of the patent "USES OF PROTEIN TYROSINE PHOSPHATASE RECEPTOR KAPPA INHIBITORS" submitted by the Université libre de Bruxelles and the Universidad Miguel Hernández de Elche (EP23382162.7, status pending). The manuscript demonstrates the interest of Protein Tyrosine Phosphatase Receptor Kappa as drug target for the treatment of HCC and therefore provides background support for the development of inhibitors targeting this specific PTP. The patent application is itself however focused on such specific PTPRK inhibitors which are not disclosed in the manuscript. The pending patent application is disclosed even if no direct impact of the publication is expected on the value of the patent application. The remaining authors declare no competing interests. E.N.G. declares that there are no other relationships or activities that might bias, or be perceived to bias, the present work.

Additional information

Supplementary information The online version contains supplementary material available at https://doi.org/10.1038/s41467-024-53733-0.

Correspondence and requests for materials should be addressed to Esteban N. Gurzov.

Peer review information *Nature Communications* thanks the anonymous reviewer(s) for their contribution to the peer review of this work. A peer review file is available.

[1]Signal Transduction and Metabolism Laboratory, Université libre de Bruxelles, B-1070 Brussels, Belgium. [2]VIB-VUB Center for Structural Biology, Vlaams Instituut voor Biotechnologie, B-1050 Brussels, Belgium. [3]Structural Biology Brussels, Vrije Universiteit Brussel, B-1050 Brussels, Belgium. [4]Brussels Center for Redox Biology, Vrije Universiteit Brussel, B-1050 Brussels, Belgium. [5]Biomolecular Mass Spectrometry and Proteomics, Bijvoet Center for Biomolecular Research and Utrecht Institute for Pharmaceutical Sciences, Utrecht University, 3584 CH Utrecht, The Netherlands. [6]Netherlands Proteomics Centre, 3584 CH Utrecht, The Netherlands. [7]Hepatology Program, CIMA, University of Navarra, 31009 Pamplona, Spain. [8]Leibniz Institute for Analytical Sciences, ISAS e.V., 44139 Dortmund, Germany. [9]Department of Gastroenterology, Hepatopancreatology and Digestive Oncology, Hôpital Universitaire de Bruxelles, B-1070 Brussels, Belgium. [10]Laboratory of Experimental Gastroenterology, Université libre de Bruxelles, B-1070 Brussels, Belgium. [11]Centre for Regenerative Medicine, Institute for Regeneration and Repair, The University of Edinburgh, Edinburgh EH16 4UU, UK. [12]Instituto de Investigación, Desarrollo e Innovación en Biotecnología Sanitaria de Elche (IDIBE), 03202 Elche, Spain. [13]IRIBHM, Université libre de Bruxelles, B-1070 Brussels, Belgium. [14]Signalling Programme, Babraham Institute, Cambridge CB22 3AT, UK. [15]Singapore Immunology Network (SIgN), Agency for Science, Technology and Research (A*STAR), Singapore 138648, Singapore. [16]Department of Pharmacy & Pharmaceutical Sciences, National University of Singapore, Singapore 117543, Singapore. [17]WELBIO Department, WEL Research Institute, B-1300 Wavre, Belgium. ✉e-mail: esteban.gurzov@ulb.be